International Journal of Mechanical Sciences 170 (2020) 105345

Contents lists available at ScienceDirect

International Journal of Mechanical Sciences

journal homepage: www.elsevier.com/locate/ijmecsci

A macroscopic description of shape memory alloy functional fatigue

Vanderson M. Dornelas[a], Sergio A. Oliveira[b], Marcelo A. Savi[a,*]

[a] Center for Nonlinear Mechanics, Department of Mechanical Engineering, Universidade Federal do Rio de Janeiro, COPPE, P.O. Box 68.503, 21.941.972 Rio de Janeiro, RJ, Brazil

[b] Department of Mechanical Engineering, CEFET/RJ – Centro Federal de Educação Tecnológica Celso Suckow da Fonseca, 20.271.110 Rio de Janeiro, RJ, Brazil

ARTICLE INFO

Keywords:
Shape memory alloys
Phase transformations
Plasticity
Transformation induced plasticity
Cyclic loading
Functional fatigue
Constitutive model
Numerical simulations

ABSTRACT

Shape memory alloys (SMAs) are smart materials employed in several applications including medical devices, aerospace components, robotics, among others. In many of these applications, devices are subjected to cyclic loading conditions. Based on this, a proper comprehension of fatigue phenomenon is essential for suitable design of systems involving SMA elements. In general, SMAs exhibit two kinds of fatigue: functional fatigue, related to the decrease of the functional properties; and structural fatigue, associated with the nucleation and growth of microcracks that lead to fracture. This paper presents a macroscopic three-dimensional constitutive model to describe functional fatigue on shape memory alloys considering continuum damage perspective. Numerical simulations are compared with experimental results showing the capabilities of the proposed model. In addition, numerical simulations are presented in order to explore the general thermomechanical aspects of SMA functional fatigue, allowing a proper comprehension of phenomenological aspects.

1. Introduction

In recent years, several researches have been carried out in materials science exploring new advanced structural systems for engineering, medicine, aerospace, robotics and other areas. Smart, adaptive or active materials are one of the most important initiatives in this field, exploiting the ability to adapt to environment using the coupling among different physical domains (mechanical, electrical, thermal, magnetic, among others). In this regard, it should be pointed out piezoelectric, electrostrictive, magnetostrictive, electro-rheological and magneto-rheological fluids, magnetic shape memory alloys and shape memory alloys [1,2].

Shape memory alloys (SMAs) are being used in several applications exploiting their remarkable properties due to solid phase transformations [3]. These alloys have complex thermomechanical behaviors and several research efforts are dedicated to investigating these behaviors considering theoretical, numerical and experimental perspectives [4,5]. The constitutive modeling of SMAs is an essential issue related to the development of this kind of material. Critical revisions about these constitutive models are available in the literature as, for instance: Lagoudas [1], Paiva and Savi [6], Khandelwal and Buravalla [7] and Cisse et al. [8].

In general, SMA applications are associated with cyclic loadings that need to be properly understood. In this regard, fatigue is an essential issue to be considered. Classically, fatigue can be divided into low cycle and high cycle fatigue. The first occurs when the material accumulates plastic strains during cyclic loading. On the other hand, high cycle fatigue occurs when the material undergoes only elastic strains. Besides, SMA fatigue presents a special type of phenomenon named functional fatigue, associated with the reduction of functional properties during cyclic loadings. Among these properties, it should be mentioned phase transformation capacity, hysteresis loop size, maximum recoverable strain and phase transformation critical stresses [9]. According to Eggeler et al. [10], many factors can affect the functional fatigue of shape memory alloys, such as temperature, microstructure, material surface quality, loading type, volume fraction, volume change during phase transformation, among others. Fig. 1 shows a schematic stress-strain curve of a NiTi alloy subjected to cyclic loading process. It should be pointed out the reduction of the critical stress transformation and the size of the hysteresis loop with the increase of the number of cycles.

Many efforts have been devoted to analyze the fatigue of shape memory alloys. Concerning experimental analysis, Tobushi et al. [11] and Figueiredo et al. [12] conducted a fatigue life investigation of NiTi wires subjected to rotational bending tests at various strain amplitudes, temperatures, rotational speeds and environment tests. Kang et al. [13] performed uniaxial experiments with controlled stress to evaluate the functional and structural fatigue of NiTi alloys. Results showed that functional and structural fatigue are directly related to the magnitude of the applied load. This result was also observed by Song et al. [14] evaluating non-proportional multiaxial loads on pseudoelastic NiTi alloys. Lagoudas et al. [15] developed an experimental analysis to evaluate the

* Corresponding author.
E-mail addresses: vm.dornelas@mecanica.coppe.ufrj.br (V.M. Dornelas), savi@mecanica.ufrj.br (M.A. Savi).

https://doi.org/10.1016/j.ijmecsci.2019.105345
Received 17 August 2019; Received in revised form 26 November 2019; Accepted 26 November 2019
Available online 4 December 2019
0020-7403/© 2019 Elsevier Ltd. All rights reserved.

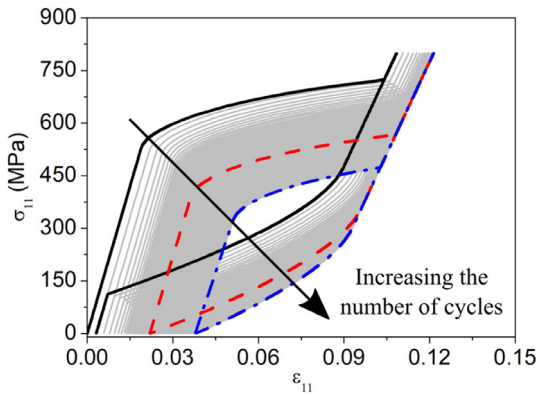

Fig. 1. Reduction of the functional properties of an SMA considering cyclic loading process.

influence of heat treatment on the fatigue life of SMA wires using an experimental apparatus where thermal cyclic tests, under different constant load levels, were performed. Bertacchini et al. [16] used a similar experimental setup to evaluate the effect of corrosive environment on SMA fatigue life. Azevedo et al. [17] employed a similar device to analyze the fatigue behavior of SMA wires subjected to thermal cycles under different, constant stress loading levels. Ramos et al. [18] discussed functional and structural fatigue of pseudoelastic NiTi wires subjected to different loading conditions considering the cycle-to-cycle pseudoelastic behavior of the material until failure. Zheng et al. [19] conducted a series of experiments on NiTi polycrystalline strips under different stress-controlled tensile loadings and frequencies with in-situ optical observation on the Lüders-band evolution. Results showed the influence of the applied stress level and frequency on the material fatigue behavior. Pelton [20] presented a literature review of the NiTi fatigue during cyclic transformations induced by thermal and mechanical loadings.

The modeling of SMA fatigue failure has been developed using essentially two main approaches: based on Coffin-Manson's empirical law, which relates the strain amplitude and the number of cycles to failure; and based on the consideration that the dissipated energy has a relation with the number of cycles until failure [18].

Considering the first approach, Tobushi et al. [21] estimated fatigue life based on strain amplitude, temperature and frequency of the cycles. Runciman et al. [22] presented a model based on an equivalent strain to estimate the number of cycles until the failure of NiTi alloys used in medical devices subjected to multiaxial loads. Maletta et al. [23] modified the Coffin-Manson equation by subdividing the strain into elastic and inelastic portions, allowing the description of the phase transformation process during cyclic loading. Kollerov et al. [24] developed a modified Coffin-Manson equation to describe and predict the fatigue behavior of NiTi alloys subjected to large strain amplitudes.

Models based on dissipated energy have been explored in different aspects. Moumni et al. [25] presented an empirical equation to estimate the number of cycles until the failure of superelastic NiTi alloys. Kan et al. [26] modified the previous model proposing a logarithmic relation. Zhang et al. [27] elaborated an extension of the original model taking into account thermomechanical couplings, which allows a more satisfactory interpretation of fatigue life experimental results. Zhang et al. [28] investigated the effect of frequency on the thermomechanical behavior and fatigue life of NiTi alloys. Zhang et al. [29] presented a stored-energy-based model for structural fatigue of shape memory alloys taking into account the conversion of hysteresis work into dissipation and stored energy.

In addition to these models, a new definition for the damage variable was proposed by Song et al. [30] to describe the fatigue evolution in NiTi microtubes subjected to uniaxial cyclic loading. Three distinct mechanisms were considered in the analysis: the phase transformation, the initiation and the propagation of microcracks. A model to predict the failure number of cycles was designed using the dissipated energy at the stabilized cycle and the dissipated energy at the *N*th cycle. Extrapolating to three-dimensional media, Song et al. [31] rewrote the damage variable taking into account non-proportional multiaxial loads, proposing a new model to predict fatigue life and comparing results with experimental data.

The constitutive modeling of functional and structural fatigue on shape memory alloys have been investigated by different perspectives. Hartl et al. [32] developed a three-dimensional constitutive model based on the continuum damage mechanics, where the damage evolution is described through a function of both the stress state and the magnitude of the transformation strain, while the complete or partial nature of the transformation cycles is also considered by experimental observations.

Barrera et al. [33] developed a macroscopic constitutive model to describe functional fatigue on shape memory alloys, being capable of simulating the training stage, the stable regime and the loss of functionality of the material. Zhang et al. [34] developed a constitutive model based on a new subdivision of the volume fractions as internal variables to control the evolution of functional fatigue during phase transformation. Bartel et al. [35] presented a phenomenological model to study functional fatigue during phase transformation of NiTi wires. In a different way of other constitutive models, volume fraction of each phase is not calculated through internal variables, but through geometric relations which evolution is obtained considering global kinetic relations.

Chemisky et al. [36] proposed a three-dimensional constitutive model to describe functional and structural damage considering the coupling between accumulation of damage and the transformation induced plasticity. This model is inspired by recent three-dimensional models for phase transformation based on the thermodynamics of irreversible processes. Phillips et al. [37] proposed a constitutive model to investigate the evolution of damage in a SMA actuator taking into account the nonlinear accumulation of damage during the SMA lifetime.

This paper aims to present a three-dimensional macroscopic constitutive model for the description of functional fatigue on shape memory alloys. The proposed model is an extension of the one proposed by Oliveira et al. [38,39], including functional fatigue. An internal variable related to continuum damage is included into the previous model together with new evolution laws. The main advantage of the proposed model over other models is the flexibility to describe different thermomechanical loads and, therefore, to be used to predict the SMA behavior in different kinds of applications. In order to verify the ability of the model to describe the functional fatigue, comparisons between numerical and uniaxial experimental results are carried out. After the verification, the model is employed to perform numerical simulations considering both uniaxial and multiaxial tests in order to explore the SMA thermomechanical behavior subjected to cyclic loading.

After this introduction, the present work is structured as follows. The constitutive model is described through the generalized standard materials formalism in Section 2. Uniaxial verification is presented in Section 3 while Section 4 discusses multiaxial numerical simulations. The conclusions are presented in Section 5.

2. Constitutive model

Shape memory alloys can be described through the generalized standard materials formalism, as presented by Lemaitre & Chaboche [40] and Coleman and Gurtin [41]. This approach is essentially based on the second law of thermodynamics establishing that the thermodynamic state of the material at a given instant is defined by a set of state variables, which are subdivided into observable and internal variables. Within this formalism, it is developed a set of constitutive equations that represents changes that occur in the thermodynamic state of the material.

The local form of the Clausius–Duhem inequality is written as follows where summation convention is evoked and the dot is the time

derivative,

$$\sigma_{ij} D_{ij} - \rho\left(\dot{\Psi} + s\dot{T}\right) - q_i g_i \geq 0 \tag{1}$$

where Ψ is the Helmholtz free energy density, ρ is the material density, s is the specific entropy, T is the temperature, σ_{ij} is the stress tensor, ε_{ij} is the total strain tensor and q_j is the heat flux. Besides, it is assumed that $D_{ij} = \dot{\varepsilon}_{ij} = \frac{1}{2}(\frac{\partial v_i}{\partial x_j} + \frac{\partial v_j}{\partial x_i})$ and $g_i = \frac{1}{T}\frac{\partial T}{\partial x_i}$, where x_i represents the spatial coordinate.

By assuming that the Helmholtz free energy density is a function of a finite set of variables, it is written as

$$\Psi = \Psi\left(\varepsilon_{ij}, \Xi, T\right) \tag{2}$$

where Ξ represents a set of internal variables. Since $\dot{\Psi} = \frac{\partial \Psi}{\partial \varepsilon_{ij}}\dot{\varepsilon}_{ij} + \frac{\partial \Psi}{\partial \Xi}\dot{\Xi} + \frac{\partial \Psi}{\partial T}\dot{T}$, the Clausius-Duhen inequality is rewritten as follows:

$$\left(\sigma_{ij} - \rho\frac{\partial \Psi}{\partial \varepsilon_{ij}}\right)\dot{\varepsilon}_{ij} - \rho\frac{\partial \Psi}{\partial \Xi}\dot{\Xi} - \rho\left(s + \frac{\partial \Psi}{\partial T}\right)\dot{T} - q_i g_i \geq 0 \tag{3}$$

This expression motivates the definitions of the thermodynamical forces, related to reversible part of the process.

$$\sigma_{ij}^R = \rho\frac{\partial \Psi}{\partial \varepsilon_{ij}};\ \mathcal{B} = -\rho\frac{\partial \Psi}{\partial \Xi};\ s = -\frac{\partial \Psi}{\partial T} \tag{4}$$

Based on that, the Clausius-Duhem inequality is given by,

$$\sigma_{ij}^I \dot{\varepsilon}_{ij} - \rho s\dot{T} - \mathcal{B}\dot{\Xi} - q_i g_i \geq 0 \tag{5}$$

Irreversible processes are described with complementary laws that can be established from a pseudo-potential of dissipation:

$$\Phi = \Phi\left(\dot{\varepsilon}_{ij}, \dot{\Xi}, q_i\right) \tag{6}$$

Therefore, thermodynamics fluxes related to irreversible process are given by:

$$\sigma_{ij}^I = \frac{\partial \Phi}{\partial \dot{\varepsilon}_{ij}};\ \mathcal{B} = \frac{\partial \Phi}{\partial \dot{\Xi}};\ g_i = -\frac{\partial \Phi}{\partial q_i} \tag{7}$$

Alternatively, thermodynamic fluxes may be obtained from the dual of the potential of dissipation $\Phi^*(\sigma_{ij}^I, \mathcal{B}, g_i)$:

$$\dot{\varepsilon}_{ij} = \frac{\partial \Phi^*}{\partial \sigma_{ij}^I};\ \dot{\Xi} = \frac{\partial \Phi^*}{\partial \mathcal{B}};\ q_i = -\frac{\partial \Phi^*}{\partial g_i} \tag{8}$$

Based on that, a complete set of constitutive equations is defined:

$$\sigma_{ij} = \rho\frac{\partial \Psi}{\partial \varepsilon_{ij}} + \frac{\partial \Phi}{\partial \dot{\varepsilon}_{ij}} \tag{9}$$

$$\mathcal{B} = -\rho\frac{\partial \Psi}{\partial \Xi} = \frac{\partial \Phi}{\partial \dot{\Xi}} \tag{10}$$

$$s = -\frac{\partial \Psi}{\partial T} \tag{11}$$

$$g_i = -\frac{\partial \Phi}{\partial q_i} \tag{12}$$

If the pseudo-potential Φ is a positive convex function that vanishes at the origin, the Clausius-Duhen inequality is automatically satisfied.

2.1. Model formulation

Inspired by the work of Oliveira et al. [38,39] that, in turn, is based on the one-dimensional model developed by Paiva et al. [42], a three-dimensional constitutive model is developed to present a macroscopic description of functional fatigue on SMAs. A new internal variable associated with functional damage is employed to this aim.

In this regard, the thermomechanical behavior of SMAs is described by assuming four macroscopic phases: austenite (A); twinned martensite (M), stable in the absence of an applied load; and two variants to present the detwinned martensite, induced by positive stress field, (M^+), and negative stress field, (M^-). These macroscopic phases are essentially related to one-dimensional media, and to take into account all possibilities of three-dimensional media, an equivalent strain field, Γ, is employed representing a phase transformation inductor responsible for the definition of the induced martensitic variant. This equivalent strain field can be defined as follows, considering indicial notation where summation convention is evoked,

$$\Gamma = \frac{1}{3}\varepsilon_{kk}^e + \frac{2}{3}\sqrt{3J_2^e}\,\mathrm{sign}\left(\varepsilon_{kk}^e\right) \tag{13}$$

where it is noticeable an influence of volumetric and deviatoric terms that are respectively given by:

$$\varepsilon_{kk}^e = \varepsilon_{11}^e + \varepsilon_{22}^e + \varepsilon_{33}^e \tag{14}$$

$$J_2^e = \frac{1}{6}\hat{\varepsilon}_{ij}^e\hat{\varepsilon}_{ij}^e = \frac{1}{6}\left\{\left(\varepsilon_{11}^e - \varepsilon_{22}^e\right)^2 + \left(\varepsilon_{22}^e - \varepsilon_{33}^e\right)^2 + \left(\varepsilon_{33}^e - \varepsilon_{11}^e\right)^2 + 6\left[\left(\varepsilon_{12}^e\right)^2 + \left(\varepsilon_{13}^e\right)^2 + \left(\varepsilon_{23}^e\right)^2\right]\right\} \tag{15}$$

Note that deviatoric elastic strain is given by:

$$\hat{\varepsilon}_{ij}^e = \varepsilon_{ij}^e - \frac{1}{3}\varepsilon_{kk}^e\delta_{ij} \tag{16}$$

and

$$\mathrm{sign}\left(\varepsilon_{kk}^e\right) = \begin{cases} +1, \text{ if } \varepsilon_{kk}^e \geq 0 \\ -1, \text{ if } \varepsilon_{kk}^e < 0 \end{cases} \tag{17}$$

where ε_{ij}^e is the elastic strain and δ_{ij} is the Kronecker delta.

Similar definitions can be done by considering the stress tensor instead of the strain. Therefore, the stress equivalent field, Γ^σ, is defined just replacing strain tensor by stress tensor in Eq. (13). Deviatoric tensor, $\hat{\sigma}_{ij}$, is defined in the same way considering Eq. (16). In addition, it is important to define the equivalent strain field related to the initial state: $\Gamma_0 = \frac{1}{3}\varepsilon_{kk}^e(0) + \frac{2}{3}\sqrt{3J_2^e(0)}\mathrm{sign}(\varepsilon_{kk}^e(0))$, where $\varepsilon_{ij}^e(0) = \varepsilon_{ij}^e - \frac{\Omega_{ij}(T-T_0)}{E_{ijkl}}$.

Under this assumption, the description of the thermodynamical state is done by considering elastic strain ε_{ij}^e, and temperature, T, and the definition of the set Ξ. It is assumed volume fractions for all macroscopic phases: β^+ related to M^+, β^- related to M^-, and β^A related to austenite (A). The fourth phase corresponds to the twinned martensite and is represented by the volume fraction β^M. Since the sum of the volume fractions is equal to unity, it is possible to write $\beta^M = 1 - \beta^+ - \beta^- - \beta^A$ and only three phases are necessary for the description. Plasticity is also contemplated in the SMA description considering both classical plasticity and transformation induced plasticity (TRIP). In this regard, hardening phenomenon is described with the aid of isotropic hardening variable, ϑ, and kinematic hardening tensor, ς_{ij}. TRIP effect is described by introducing the internal variables ξ^+, ξ^- and ξ^A, which are related to saturation effect during the cyclic loadings.

The constitutive model formulation follows the same approach developed by Oliveira et al. [39], incorporating the functional fatigue by considering an extra internal variable, D_f, which represents continuum damage. Essentially, this variable describes the local damage representing the loss of actuation being associated with damaged material state. The damaged state is characterized by $0 \leq D_f < 1$, where $D_f = 0$ represents the undamaged material and $D_f = 1$ is a material state that is not able to perform any actuation. Phenomenologically speaking, the functional damage evolution is dependent on the stress level and phase transformations.

Based on these assumptions, it is possible to write a Helmholtz free energy density for the mixture of all phases as follows [39]:

$$\begin{aligned}
&\rho\Psi\left(\varepsilon_{ij}^e, T, \vartheta, \varsigma_{ij}, D_f,\ \beta^+, \beta^-,\ \beta^A, \xi^+, \xi^-, \xi^A\right) = \Gamma\alpha\left(\beta^- - \beta^+\right) - \\
&-\left(1 - D_f\right)\Lambda\left(\beta^+ + \beta^-\right) + \left[\frac{1}{2}\left(E_{ijkl}^A - E_{ijkl}^M\right)\varepsilon_{ij}^e\varepsilon_{kl}^e - \left(1 - D_f\right)\Lambda^{\aleph} - \right. \\
&\left. -\left(\Omega_{ij}^A - \Omega_{ij}^M\right)\left(T - T_0\right)\varepsilon_{ij}^e + \frac{1}{2}\left(K^A - K^M\right)\vartheta^2 + \left(\frac{1}{2H^A} - \frac{1}{2H^M}\right)\varsigma_{ij}\varsigma_{ij}\right]\beta^A + \\
&+\frac{1}{2}E_{ijkl}^M\varepsilon_{ij}^e\varepsilon_{kl}^e + \left(1 - D_f\right)\Lambda^M - \Omega_{ij}^M\left(T - T_0\right)\varepsilon_{ij}^e + \frac{1}{2}K^M\vartheta^2 + \\
&+\frac{1}{2H^M}\varsigma_{ij}\varsigma_{ij} + I_\pi\left(\beta^+,\ \beta^-,\ \beta^A\right)
\end{aligned} \tag{18}$$

The indicator function, I_π, is used in order to establish proper phase coexistence constraints, defining a convex set π associated with phase volume fractions.

Besides, the previous equation considers that superscript A is related to austenite, M to martensite; index + is related to tension detwinned martensite, M^+, while index – is associated with compression detwinned martensite, M^-; T_0 is a reference temperature in a stress-free state.

It should be pointed out that functional damage appears in the free energy density in order to alter phase transformation capacity. The idea is similar to the classical continuum damage theory [40] where the damage changes the effective macroscopic phenomena. Specifically for SMAs, functional damage reduces the effective phase transformation critical stress.

Based on the generalized standard material approach, thermodynamic forces are defined from the free energy density, Eq. (18), as presented in the previous section and generally represented by the set $\mathcal{B}$ in Eq. (4). The same approach developed by Oliveira et al. [39] is employed, considering the following thermodynamical forces: B^+, $B^-$and B^A are the forces related to phase transformation; X_{ij}, Y and Z_{ij} refer to classical plasticity; F^{D_f} is the thermodynamic force associated with functional damage; R_{ij}, S^+, $S^-$and S^A are associated with the TRIP effect, being responsible for changes of the parameter nominal values representing the saturation effect.

After the definition of thermodynamical forces, dissipative behavior is described considering the dual of the pseudo-potential of dissipation that can be written as follows:

$$\begin{aligned}\bar{\Phi}^M\left(X_{ij}, Y, Z_{ij}, R_{ij}, F^{D_f}, B^+, B^-, B^A, S^+, S^-, S^A\right) &= \frac{1}{2\eta^+}\left(B^+ + \eta^I Y + \right.\\ &\left.+\eta^K_{ij} Z_{ij}\right)^2 + \frac{1}{2\eta^-}\left(B^- + \eta^I Y + \eta^K_{ij} Z_{ij}\right)^2 + \frac{1}{2\eta^A}\left(B^A - \eta^I Y - \eta^K_{ij} Z_{ij}\right)^2 + \\ &+R_{ij} R_{ij}\left\{\left(M_{13}\beta^+ + M_{31}\beta^A\right)\dot{\beta}^+ + \left(M_{32}\beta^- + M_{23}\beta^A\right)\dot{\beta}^- + \right.\\ &\left.+\left[M_{43}\beta^A + M_{34}\left(1 - \beta^+ - \beta^- - \beta^A\right)\right]\dot{\beta}^A\right\} + \left|\dot{\beta}^+\right| S^+ + \\ &+\left|\dot{\beta}^-\right| S^- + \left|\dot{\beta}^A\right| S^A + F^{D_f}\left[\left(C_1 + C_2\Gamma^\sigma\right)^{c_3}\left(\left|\dot{\beta}^+\right| + \left|\dot{\beta}^-\right| + \left|\dot{\beta}^A\right|\right)\right] + \\ &+I_f\left(X_{ij}, Y, Z_{ij}, R_{ij}, S^+, S^-, S^A\right) + I_{\bar{\chi}}\left(B^+, B^-, B^A\right)\end{aligned} \tag{19}$$

An indicator function $I_{\bar{\chi}}$ is employed in order to establish constraints related to phase transformations, defining a convex set $\bar{\chi}$. Alternatively, a dual set, χ, is proposed based on the state variables instead of thermodynamic forces.

It should be pointed out that the functional damage is directly related to the term $F^{D_f}[(C_1 + C_2\Gamma^\sigma)^{c_3}(|\dot{\beta}^+| + |\dot{\beta}^-| + |\dot{\beta}^A|)]$. Therefore, the damage evolution should be induced by phase transformations, which means that the more phase transformations occur the more functional damage accumulates. It can be understood as an accumulated phase transformation that is proportional to the applied stress level.

Complementary evolution laws are defined from the pseudo-potential of dissipation, Eq. (19). Under these assumptions, the generalized standard material formalism establishes a complete set of equations to describe the thermomechanical behavior of SMAs, including four macroscopic phases, tension-compression asymmetry, classical plasticity, transformation induced plasticity and functional damage.

The development for obtaining the constitutive equations employs convex analysis framework that uses the concept of sub-differentials that is essentially similar to the use of Lagrange multipliers. Either phase transformation or plasticity is analogous in the sense and sub-differentials can be understood as projections to the feasible domain. The domain of phase transformation phenomenon is related to volume fraction space, respecting the phase coexistence criterion. Plasticity domain, on the other hand, is related to the yield surface space. The next section presents the constitutive equations.

2.2. Constitutive equations

The complete set of constitutive equations is presented in the sequence.

Stress-strain-temperature relation:

$$\sigma_{ij} = E_{ijkl}\varepsilon^e_{kl} + \alpha\omega_{ij}\left(\beta^- - \beta^+\right) - \Omega_{ij}\left(T - T_0\right) \tag{20}$$

Evolution equations for the volume fractions:

$$\begin{aligned}\dot{\beta}^+ = \frac{1}{\eta^+}\Big\{&\alpha\Gamma + \left(1 - D_f\right)\Lambda + P^+ - \alpha^h_{ijkl} r_{kl}\Omega_{ij}\left(T - T_0\right) \\ &-\eta^I K\vartheta - \eta^K_{ij}\frac{\varsigma_{ij}}{H} - \kappa^+_\pi\Big\} + \kappa^+_\chi\end{aligned} \tag{21}$$

$$\begin{aligned}\dot{\beta}^- = \frac{1}{\eta^-}\Big\{&-\alpha\Gamma + \left(1 - D_f\right)\Lambda + P^- + \alpha^h_{ijkl} r_{kl}\Omega_{ij}\left(T - T_0\right) \\ &-\eta^I K\vartheta - \eta^K_{ij}\frac{\varsigma_{ij}}{H} - \kappa^-_\pi\Big\} + \kappa^-_\chi\end{aligned} \tag{22}$$

$$\begin{aligned}\dot{\beta}^A = \frac{1}{\eta^A}\Big\{&\left(1 - D_f\right)\Lambda^\aleph + P^A + \varepsilon^e_{ij}\left(\Omega^A_{ij} - \Omega^M_{ij}\right)\left(T - T_0\right) \\ &-\frac{1}{2}\left(K^A - K^M\right)\vartheta^2 - \left(\frac{1}{2H^A} - \frac{1}{2H^M}\right)\varsigma_{ij}\varsigma_{ij} \\ &+\eta^I K\vartheta + \eta^K_{ij}\frac{\varsigma_{ij}}{H} - \kappa^A_\pi\Big\} + \kappa^A_\chi\end{aligned} \tag{23}$$

Evolution equation for the functional damage:

$$\dot{D}_f = \left(C_1 + C_2\Gamma^\sigma\right)^{C_3}\left(\left|\dot{\beta}^+\right| + \left|\dot{\beta}^-\right| + \left|\dot{\beta}^A\right|\right) \tag{24}$$

Evolution equations for plasticity:

$$\dot{\varepsilon}^p_{ij} = \gamma\frac{\hat{\sigma}_{ij} - \varsigma_{ij}}{||\hat{\sigma}_{ij} - \varsigma_{ij}||} \tag{25}$$

$$\dot{\vartheta} = \sqrt{\frac{2}{3}}\gamma + \eta^I\left(\dot{\beta}^+ + \dot{\beta}^- + \dot{\beta}^A\right);\ \dot{\varsigma}_{ij} = \frac{2}{3}H\dot{\varepsilon}^p_{ij} + \eta^K_{ij}\left(\dot{\beta}^+ + \dot{\beta}^- + \dot{\beta}^A\right) \tag{26}$$

Evolution equations for TRIP:

$$\begin{aligned}\dot{\varepsilon}^{trip}_{ij} = 2\sigma_{ij}\Big\{&\left(M_{13}\beta^+ + M_{31}\beta^A\right)\dot{\beta}^+ + \left(M_{32}\beta^- + M_{23}\beta^A\right)\dot{\beta}^- \\ &+\left[M_{43}\beta^A + M_{34}\left(1 - \beta^+ - \beta^- - \beta^A\right)\right]\dot{\beta}^A\Big\}\end{aligned} \tag{27}$$

$$\dot{\xi}^+ = \left|\dot{\beta}^+\right|;\ \dot{\xi}^- = \left|\dot{\beta}^-\right|;\ \dot{\xi}^A = \left|\dot{\beta}^A\right| \tag{28}$$

Yield surface and its conditions:

$$f = ||\hat{\sigma}_{ij} - \varsigma_{ij}|| - \sqrt{\frac{2}{3}}\left(\sigma_Y - K\vartheta\right) \tag{29}$$

$$\gamma \geq 0;\ f \leq 0 \text{ and } \gamma f = 0;\ \gamma\dot{f} = 0 \text{ if } f = 0 \tag{30}$$

where γ is the plastic multiplier associated with the indicator function I_f, related to the yield surface set.

Phase transformation constraints:

$\kappa_\pi(\beta^+,\beta^-,\beta^A)$ – phase coexistence constraints associated with the convex set π,

$$\pi = \left\{\beta^m \,\middle|\, 0 \leq \beta^m \leq 1(m = +, -, A); \beta^+ + \beta^- + \beta^A \leq 1\right\} \tag{31}$$

$\kappa_\chi = \kappa_\chi(\dot{\beta}^+, \dot{\beta}^-, \dot{\beta}^A)$ – phase transformation constraints establishing conditions for internal sub-loops due to incomplete phase transformations associated with the convex set χ defined for mechanical loadings and thermal loadings from its subsets.

Phase transformations governed by mechanical loadings, $\dot{\Gamma}^\sigma \neq 0$:

$$\chi = \left\{\dot{\beta}^n \,\middle|\, \begin{array}{l}\dot{\Gamma}\dot{\beta}^+ \geq 0;\ \dot{\Gamma}\dot{\beta}^A \leq 0\ if\ \Gamma_0 > 0 \\ \dot{\Gamma}\dot{\beta}^- \leq 0;\ \dot{\Gamma}\dot{\beta}^A \geq 0\ if\ \Gamma_0 < 0\end{array}\right\} \tag{32}$$

Phase transformations governed by thermal loadings, $\dot{\Gamma}^\sigma = 0$ (subsets χ_1, χ_2, χ_3):

$$\chi_1 = \left\{\dot{\beta}^n \,\middle|\, \dot{T}\dot{\beta}^A \geq 0\right\} \tag{33}$$

$$\chi_2 = \left\{\dot{\beta}^n \,\middle|\, \dot{T}\dot{\beta}^+ = 0\left[\begin{array}{l}\text{if } \dot{T} > 0,\ \dot{\beta}^+ > 0 \text{ and } \beta^+_s \neq 0 \\ \text{if } \dot{T} > 0,\ \beta^+ \neq \beta^+_s \text{ and } \beta^+_s = 0 \\ \text{if } \dot{T} > 0,\ \dot{\beta}^A = 0 \\ \textit{if } \dot{T} < 0,\ \Gamma^\sigma = 0 \textit{ and } \beta^+ \neq \beta^+_s\end{array}\right.\right\} \tag{34}$$

$$\chi_3 = \left\{ \dot{\beta}^n \;\middle|\; \dot{T}\dot{\beta}^- = 0 \left[\begin{array}{l} \text{if } \dot{T} > 0,\ \dot{\beta}^- > 0 \text{ and } \beta_s^- \neq 0 \\ \text{if } \dot{T} > 0,\ \beta^- \neq \beta_s^- \text{ and } \beta_s^- = 0 \\ \text{if } \dot{T} > 0,\ \dot{\beta}^A = 0 \\ \textit{if } \dot{T} < 0\ \Gamma^\sigma = 0 \textit{ and } \beta^- \neq \beta_s^- \end{array} \right. \right\} \tag{35}$$

where β_s^+ and β_s^- are the values of β^+ and β^-, respectively, when the phase transformation begins.

2.3. Parameters

After the presentation of the constitutive equations, further explanations are provided in the sequence. Damage description considers the function $(C_1 + C_2\Gamma^\sigma)^{C_3}$ in order to establish the relation between damage and accumulated phase transformation, making it proportional to the equivalent stress field, Γ^σ. This function has a phenomenological inspiration, being able to capture the main features of the functional fatigue. Therefore, parameters C_1, C_2 and C_3 define the main characteristic of functional damage evolution.

Concerning thermoelastic parameters, E_{ijkl} is the elastic tensor defined according to the classical theory of elasticity; Ω_{ij} is a tensor related to the thermal expansion coefficients. Both tensors have the same general form, representing a kind of rule of mixtures between austenitic and martensitic properties: $E_{ijkl} = E^M_{ijkl} + \beta^A(E^A_{ijkl} - E^M_{ijkl})$ and $\Omega_{ij} = \Omega^M_{ij} + \beta^A(\Omega^A_{ij} - \Omega^M_{ij})$.

Phase transformation parameters are represented by α, that controls the height of the stress–strain hysteresis loop; Λ and $\Lambda^\aleph$ are temperature functions that define the stress value for the phase transformation.

$$\left(\widetilde{\eta_L^+}\right)_{ijkl} \equiv \begin{bmatrix} (\eta_L^+)_N & (\eta_L^+)_N - (\eta_L^+)_S & (\eta_L^+)_N - (\eta_L^+)_S & 0 & 0 & 0 \\ (\eta_L^+)_N - (\eta_L^+)_S & (\eta_L^+)_N & (\eta_L^+)_N - (\eta_L^+)_S & 0 & 0 & 0 \\ (\eta_L^+)_N - (\eta_L^+)_S & (\eta_L^+)_N - (\eta_L^+)_S & (\eta_L^+)_N & 0 & 0 & 0 \\ 0 & 0 & 0 & 2(\eta_L^+)_S & 0 & 0 \\ 0 & 0 & 0 & 0 & 2(\eta_L^+)_S & 0 \\ 0 & 0 & 0 & 0 & 0 & 2(\eta_L^+)_S \end{bmatrix} \tag{43}$$

$$\Lambda = 2\Lambda^M = \begin{cases} -L_0^\pm + \dfrac{L^\pm}{T^M}\left(T - T^M\right) \text{ if } T > T^M \\ -L_0^\pm \text{ if } T \leq T^M \end{cases} \tag{36}$$

$$\Lambda^\aleph = \Lambda^M + \Lambda^A = \begin{cases} -L_0^A + \dfrac{L^A}{T^M}\left(T - T^M\right) \text{ if } T > T^M \\ -L_0^A \text{ if } T \leq T^M \end{cases} \tag{37}$$

where T^M is the temperature below which the martensitic phase becomes stable for a stress-free state; note that the phase transformation stress level is constant for $T < T^M$. It should be pointed out that Λ^M and Λ^A are the stress phase transformation values for each isolated phase, martensite and austenite, respectively.

Besides, α^h_{ijkl} is a fourth-order tensor that controls the stress-strain hysteresis loop width. Due to symmetry assumptions, α^h_{ijkl} can be represented by a matrix considering the parameters α^h_N and α^h_S, related to normal and shear behaviors respectively, similar to the isotropic elastic tensor.

$$\alpha^h_{ijkl} \equiv \begin{bmatrix} \alpha^h_N & \alpha^h_N - \alpha^h_S & \alpha^h_N - \alpha^h_S & 0 & 0 & 0 \\ \alpha^h_N - \alpha^h_S & \alpha^h_N & \alpha^h_N - \alpha^h_S & 0 & 0 & 0 \\ \alpha^h_N - \alpha^h_S & \alpha^h_N - \alpha^h_S & \alpha^h_N & 0 & 0 & 0 \\ 0 & 0 & 0 & \alpha^h_S & 0 & 0 \\ 0 & 0 & 0 & 0 & \alpha^h_S & 0 \\ 0 & 0 & 0 & 0 & 0 & \alpha^h_S \end{bmatrix} \tag{38}$$

In addition, r_{kl} is a symmetric second-order tensor related to the loading history, defined as:

$$r_{kl} = \begin{cases} +1, & \text{if } \sigma_{kl} > 0 \\ 0, & \text{if } \sigma_{kl} = 0 \\ -1, & \text{if } \sigma_{kl} < 0 \end{cases} \tag{39}$$

Taking into account non-simultaneous multiaxial loadings, r_{kl} is written for the subsequent loadings (assuming stress driving cases):

$$r_{kl} = \frac{\sigma_{kl}}{\left|S^{\max}_{kl}\right|} \text{ if } \beta^+ \neq 0 \text{ or } \beta^- \neq 0 \tag{40}$$

where $S^{\max}_{kl}$ is the maximum value of the mechanical loading that can be a stress or a strain. Moreover, note that $\frac{\sigma_{kl}}{|S^{\max}_{kl}|} = 0$ if $S^{\max}_{kl} = 0$.

The parameters $\eta^m (m = +, -, A)$ are associated with the internal dissipation of the material and can be expressed considering different values in the following form:

$$\begin{cases} \eta^\pm = \eta^\pm_L \text{ if } \dot{\Gamma} > 0 \\ \eta^\pm = \eta^\pm_U \text{ if } \dot{\Gamma} < 0 \end{cases}; \qquad \begin{cases} \eta^A = \eta^A_L \text{ if } \dot{\Gamma} > 0 \\ \eta^A = \eta^A_U \text{ if } \dot{\Gamma} < 0 \end{cases} \tag{41}$$

where each one the parameters η^+_L, η^-_L, η^+_U, η^-_U, η^A_L and η^A_U are calculated considering the use of fourth-order tensors. In order to explain this approach, consider parameter η^+_L that is given by

$$\begin{cases} \eta^+_L = r_{ij}\left(\widetilde{\eta^+_L}\right)_{ijkl} r_{kl} & \text{if } \Gamma^\sigma \neq 0 \\ \eta^+_L = \left(\eta^+_L\right)_N & \text{otherwise} \end{cases} \tag{42}$$

where

where $(\eta^+_L)_N$ and $(\eta^+_L)_S$ represents normal and shear components of the specific parameter. Similar definitions are employed for the other parameters, η^-_L, η^+_U, η^-_U, η^A_L and η^A_U.

Concerning classical plasticity parameters, K is plastic modulus; H is the kinematic hardening modulus. Once again, both parameters are defined considering a rule of mixture: $K = K^M + \beta^A(K^A - K^M)$ and $\frac{1}{H} = \frac{1}{H^M} + \beta^A(\frac{1}{H^A} - \frac{1}{H^M})$.

Besides, η^I defines the coupling between phase transformation and isotropic hardening. The coupling between phase transformation and kinematic hardening is defined by the second-order tensor $\eta^K_{ij} \equiv \eta^K \begin{bmatrix} 1 & 1 & 1 \\ 1 & 1 & 1 \\ 1 & 1 & 1 \end{bmatrix}$

The yield stress σ_Y has different values for austenitic and martensitic phases. Their values are also temperature dependent and can be written as follows:

$$\begin{cases} \sigma_Y = \sigma^M_Y \text{ if } T \leq T^M \\ \sigma_Y = \dfrac{\sigma^M_Y\left(T^A - T\right) + \sigma^{Ai}_Y\left(T - T^M\right)}{T^A - T^M} \text{ if } T^M < T \leq T^A \\ \sigma_Y = \dfrac{\sigma^{Ai}_Y\left(T^F - T\right) + \sigma^{Af}_Y\left(T - T^A\right)}{T^F - T^A} \textit{ if } T^M < T \leq T^F \end{cases} \tag{44}$$

where T^A is the temperature above which the austenitic phase is stable; T^F is a reference temperature for the determination of the yield stress for high temperatures; σ^M_Y is yield stress of the martensitic phase;

Table 1.
Parameters obtained from the experimental results developed by Ramos et al. [18].

E^A (GPa)	E^M (GPa)	Ω^A (MPa/K)	Ω^M (MPa/K)	α_N^h(MPa)	$\hat{\alpha}$(MPa)
32.0	22.0	0.74	0.17	0.059	80.0
$\hat{L}_0^{\pm}$(MPa)	$\hat{L}^{\pm}$ (MPa)	$\hat{L}_0^A$(MPa)	$\hat{L}^A$ (MPa)	$(\eta_L)_N$(MPa.s)	$(\eta_U)_N$(MPa.s)
18.0	10.0	0.6	160.0	0.125	0.700
$(\eta_L^A)_N$ (MPa.s)	$(\eta_U^A)_N$(MPa.s)	T^M (K)	T^A (K)	σ_Y^M (GPa)	σ_Y^{Ai} (GPa)
0.125	0.700	275.0	282.0	0.5	1.5
σ_Y^{Af} (GPa)	K^A (GPa)	K^M (GPa)	H^A (GPa)	H^M (GPa)	η^I
1.0	1.4	0.4	4.0	1.1	− 0.01
η^K	T^F (K)	$\hat{M}_{13}$ (GPa^{-1})	$\hat{M}_{31}$(GPa^{-1})	$\hat{M}_{32}$(GPa^{-1})	$\hat{M}_{23}$ (GPa^{-1})
− 0.01	423.0	0.12	0.05	0.12	0.05
T^{trip}(K)	m^α	m^L	m^M	N	C_1
290.0	0.900	0.03	0.095	3	2×10^{-6}
C_2	C_3				
4×10^{-12}	1.58				

σ_Y^{Ai} and σ_Y^{Af} define the thermal variation of the yield stress of the austenitic phase.

TRIP effect is associated with the parameters $M_{13}, M_{31}, M_{23}, M_{32}, M_{34}$ and M_{43}. They have a saturation characteristic defined from TRIP variables: $M_{ij} = \hat{M}_{ij}\exp(-m^M \xi^i)$, where m^M is a saturation parameter. In order to control the amount of TRIP strain at different temperatures, the following expressions are employed:

$$\hat{M}_{ij} = \begin{cases} 0 \text{ if } T < T^{trip} \\ \hat{M}_{ij}^R \dfrac{(T - T^{trip})}{(T^F - T^{trip})} \text{ if } T \geq T^{trip} \end{cases} \tag{45}$$

where $\hat{M}_{ij}^R$ is a reference value of $\hat{M}_{ij}$ at $T = T^{trip}$ and T^{trip} is a temperature below which TRIP should not occur.

Besides, other parameters as α, L_o^+, L_o^-, L_o^A, L^+, L^-, L^A, also presents a saturation characteristic as follows: $(\,) = \widehat{(\,)}[\frac{N+\exp(-m^{(\,)}\xi^{\pm})}{N+1}]$, where N provides a proper adjustment.

Auxiliary variables are also employed to present the constitutive equations, being defined as follows:

$$\omega_{ij} = \frac{1}{3}\delta_{ij} + \left[\frac{3\varepsilon_{ij}^e - \varepsilon_{kk}^e\delta_{ij}}{3\sqrt{3J_2^e}}\right]\text{sign}(\varepsilon_{kk}^e) \tag{46}$$

$$P^+ = +E_{ijkl}\varepsilon_{kl}^e\alpha_{ijpq}^h r_{pq} + \alpha(\beta^- - \beta^+)\left[\frac{1}{3}\alpha_{iikl}^h r_{kl} + \frac{2\ P^\alpha}{\sqrt{3J_2^e}}\text{sign}(\varepsilon_{kk}^e)\right] \tag{47}$$

$$P^- = -E_{ijkl}\varepsilon_{kl}^e\alpha_{ijpq}^h r_{pq} - \alpha(\beta^- - \beta^+)\left[\frac{1}{3}\alpha_{iikl}^h r_{kl} + \frac{2\ P^\alpha}{\sqrt{3J_2^e}}\text{sign}(\varepsilon_{kk}^e)\right] \tag{48}$$

$$P^A = -\frac{1}{2}E_{ijkl}^A\varepsilon_{ij}^e\varepsilon_{kl}^e + \frac{1}{2}E_{ijkl}^M\varepsilon_{ij}^e\varepsilon_{kl}^e \tag{49}$$

$$P^\alpha = \frac{\alpha_S^h}{6}\Big[(r_{11} - r_{22})(\varepsilon_{11}^e - \varepsilon_{22}^e) + (r_{22} - r_{33})(\varepsilon_{22}^e - \varepsilon_{33}^e) + (r_{33} - r_{11})(\varepsilon_{33}^e - \varepsilon_{11}^e) + 6(r_{12}\varepsilon_{12}^e + r_{13}\varepsilon_{13}^e + r_{23}\varepsilon_{23}^e)\Big] \tag{50}$$

For more details about model parameters, see Oliveira et al. [38,39]. Numerical procedure employs the same strategy of the one presented in Oliveira et al. [38,39] and Paiva et al. [42]. Basically, the solution of the constitutive equations is obtained through the operator split technique [43], which makes it possible to solve a set of coupled equations by uncoupled problems. Therefore, two numerical procedures associated with phase transformation and plastic behavior are used. The evolution of the constitutive equations is evaluated by an implicit Euler method. Concerning sub-differential evaluations, the equations are evaluated neglecting them. Afterward, the thermodynamical state is verified, checking all the constraints. If the thermodynamical state is not feasible, sub-differentials are calculated from a projection on state variables space. Note that, in this sense, phase transformation constraints are similar to plastic ones. Plastic multiplier is related to a sub-differential associated with yield surface, while phase transformation constraints are related to phase space. For more details about the numerical procedure see Oliveira et al. [38].

In the sequence, numerical simulations are carried out. Initially, model verification is performed considering cyclic uniaxial tests. Two situations are considered: mechanical loading and thermal loading. Afterward, model capability to describe multiaxial tests is of concern considering numerical simulations related to different thermomechanical loadings.

3. Uniaxial tests

Numerical simulations of uniaxial tests are now of concern. The proposed model contemplates a set of parameters that are adjusted through experimental tests. Classical parameters from elasticity and plasticity theories are estimated, as usual, considering different values

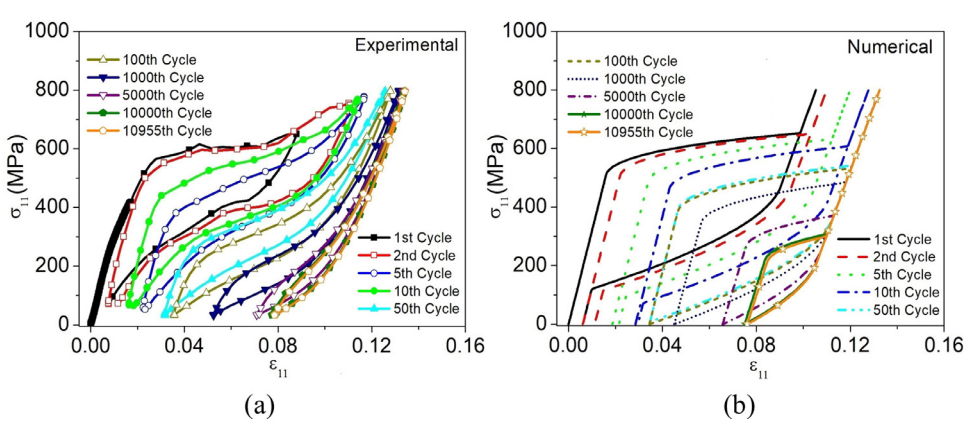

Fig. 2. Pseudoelastic functional fatigue considering cyclic test performed by Ramos et al. [18]: (a) experimental data; (b) numerical results.

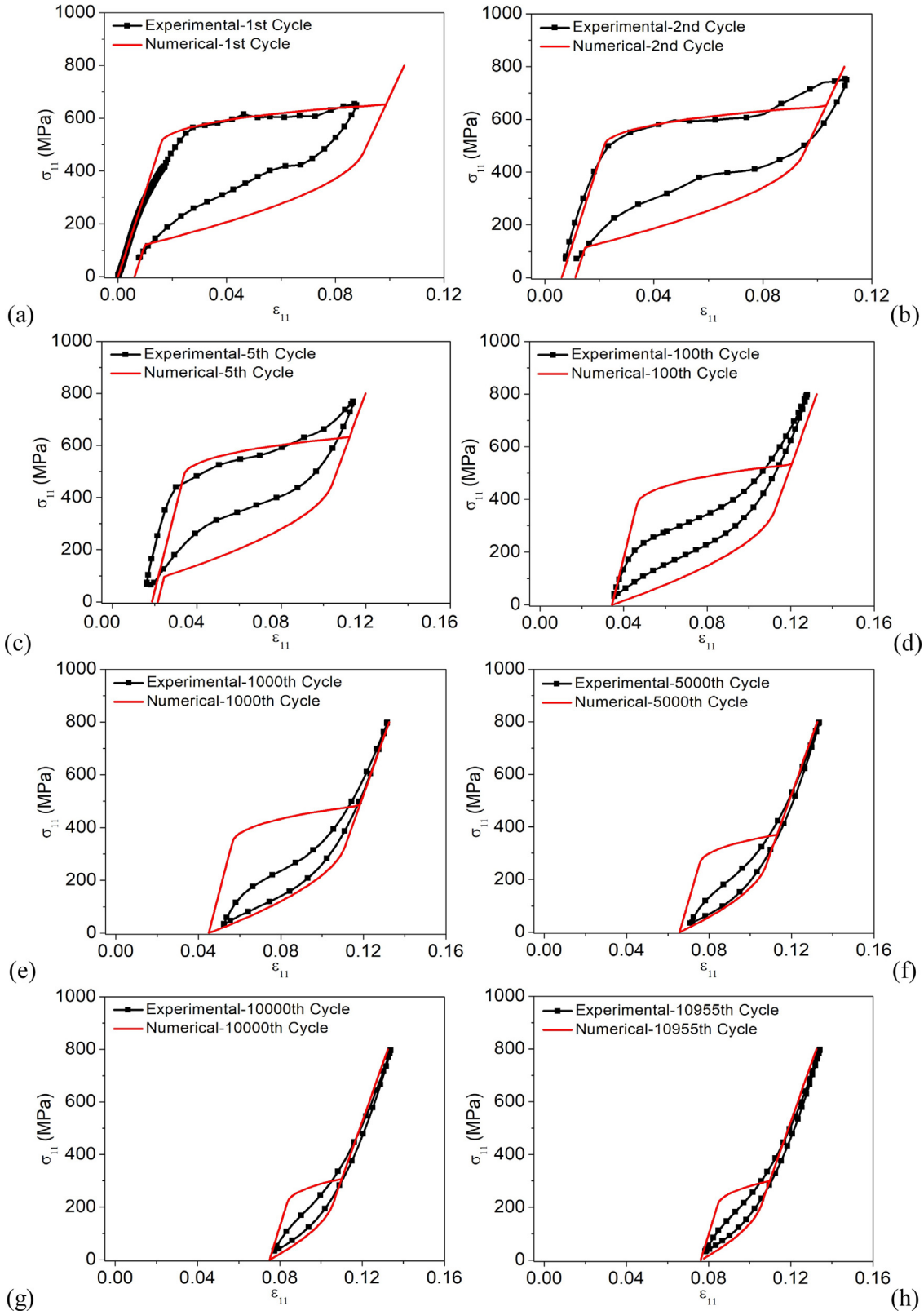

Fig. 3. Pseudoelastic behavior with functional damage based on the experimental test performed by Ramos et al. [18]. Numerical-experimental comparative for different cycles: (a) 1st cycle; (b) 2nd cycle; (c) 5th cycle; (d) 100th cycle; (e) 1,000th cycle; (f) 5,000th cycle; (g) 10,000th cycle; (h) last (10,955th) cycle.

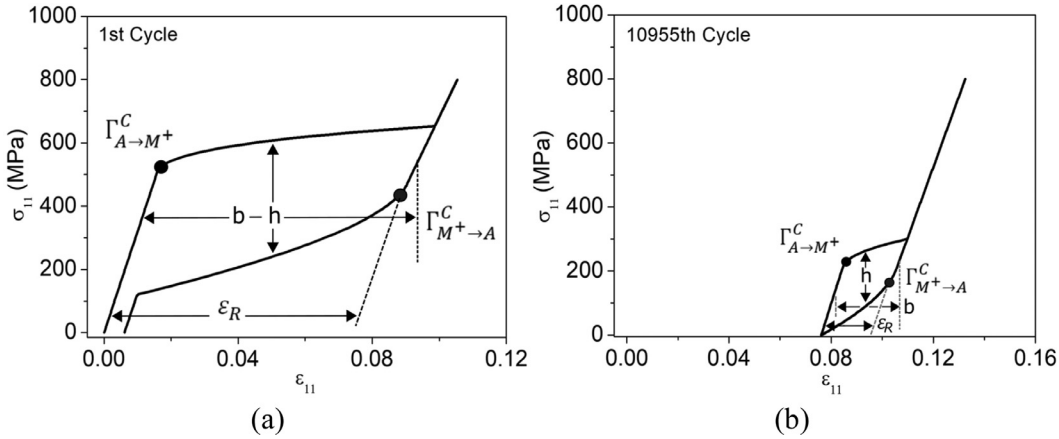

Fig. 4. Characteristic parameters that characterize the stress-strain hysteresis loop employed to evaluate functional fatigue: (a) first cycle; (b) last (10,955th) cycle.

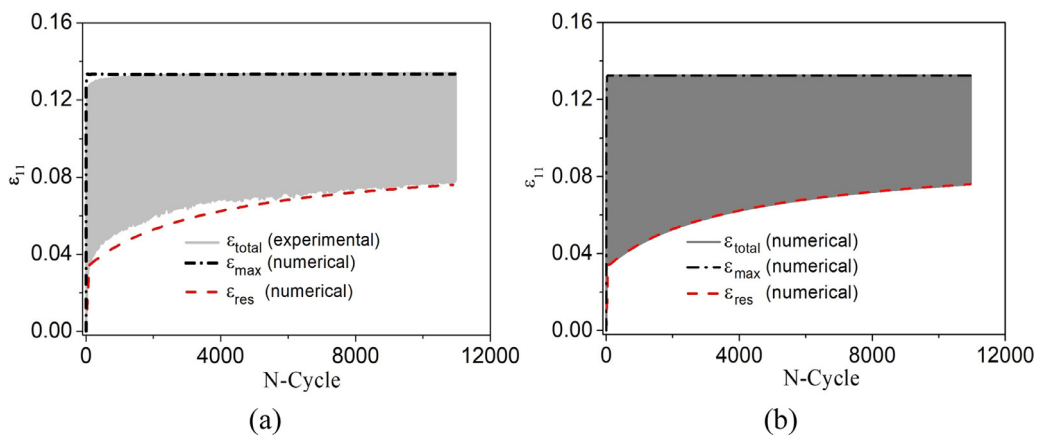

Fig. 5. Strain evolution through the cyclic tests to evaluate functional fatigue: (a) experimental test due to Ramos et al. [18]; (b) numerical simulations.

Table 2.
Characteristics of the 1st and 10,955th stress-strain loops.

	1st cycle	10,955th cycle	Variation (%)
$\Gamma^C_{A\to M^+}$ (MPa)	518.0	220.5	−57.4
$\Gamma^C_{M^+\to A}$ (MPa)	457.7	190.9	−58.3
h (MPa)	361.3	162.8	−54.9
b	0.08	0.02	−75.0
ε_R	0.07	0.02	−71.4

for austenitic and martensitic phases. The remaining parameters are adjusted in order to match experimental data. Experimental tests performed by Ramos et al. [18] are used as a reference and the adjusted parameters are presented in Table 1. Basically, pseudoelastic NiTi SMA wires of 0.5 mm diameter are subjected to cyclic tension tests with peak stress of 800 MPa (without reaching the yield surface), with frequency of 2 Hz, at room temperature.

Experimental results due to Ramos et al. [18] are presented in Fig. 2(a) in the form of stress-strain curves for 10,955 cycles. In general, it is observed a progressive decrease in the functional properties of the material, altering the position and characteristic of the hysteresis loop. This behavior is known as functional fatigue since it reduces the SMA actuation capacity. In brief, functional fatigue is related to a loss of actuation performance, which can be estimated through hysteresis characteristics. Fig. 2(b) presents numerical simulations obtained from the proposed model of the same test, showing a good agreement between them. Fig. 3 shows a comparison between numerical and experimental curves for some specific cycles. These results present the evidence that the SMA model is able to capture the general thermomechanical behavior related to functional fatigue.

Since functional fatigue is a loss of actuation performance, an analysis of hysteresis characteristics allows one to have a proper comprehension of the phenomenon. Fig. 4 shows hysteresis characteristics for the first and last (10,955th) cycles of the test. Measured values are presented in Table 2 showing that functional fatigue and TRIP effect promotes a reduction around 60% of critical stresses. The other hysteresis loop characteristics show a reduction from 50 to 75% affecting the material functionality.

Fig. 5 shows a numerical-experimental comparison of the strain evolution through the cycles. This analysis considers that total strain can be observed from two parts: maximum strain ($\varepsilon_{\max}$), representing the maximum strain value during the loading process; and residual strain (ε_{res}), related to the residual strain after the finish of the loading process. Fig. 5(a) presents the experimental data due to Ramos et al. [18], together with numerical results of maximum strain and residual strain. Fig. 5(b) shows the same test performed by numerical simulations. It should be pointed out the good agreement between numerical and experimental results, showing the model capability to describe the evolution of functional damage during cyclic loading process.

The evolution of volume fractions is now of concern in order to show the actuation lost from a phase transformation perspective. Considering a pseudoelastic test where positive stresses are inducing phase transformations, the volume fractions of twinned martensite (M) and detwinned martensite induced by negative stress field (M^-) vanish. Fig. 6 shows volume fractions evolution for different cycles: 1st, 1,000th, 5,000th and 10,955th. Initially, it is observed that the material has 100% of its

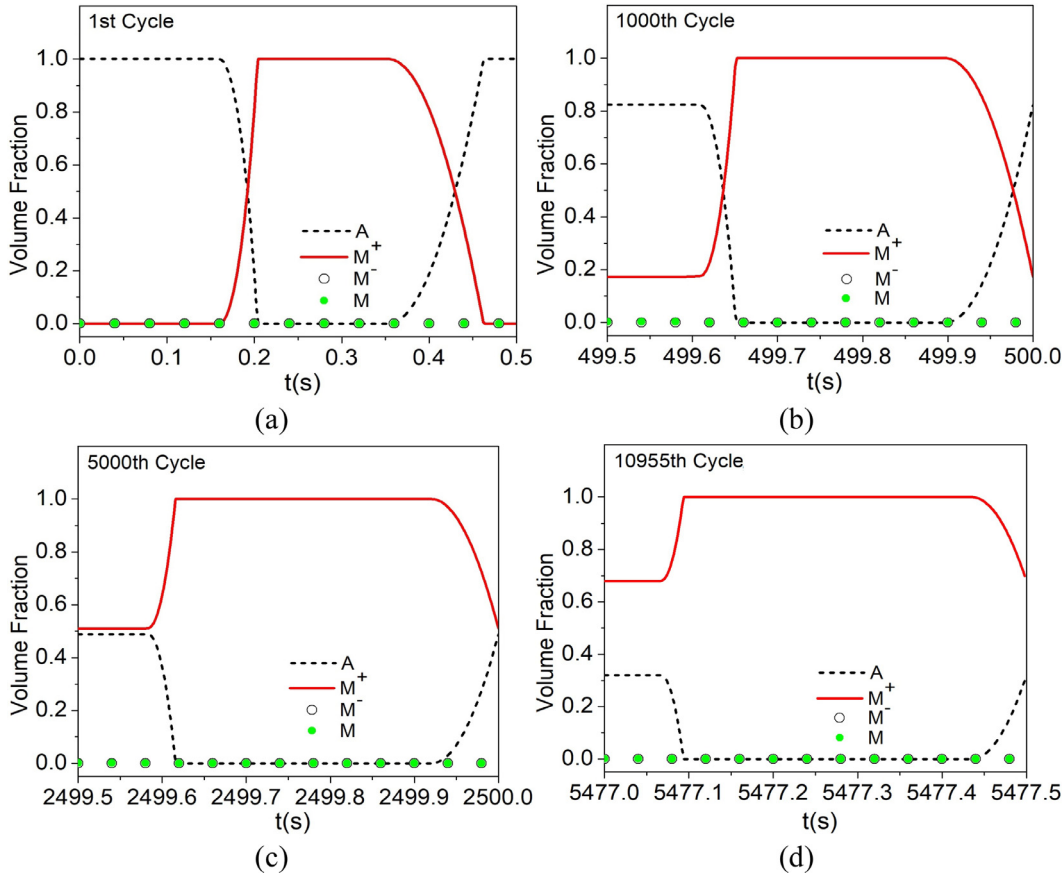

Fig. 6. Evolution of volume fractions through different cycles to evaluate functional fatigue: (a) 1st cycle; (b) 1,000th cycle; (c) 5,000th cycle; (d) 10,955th cycle.

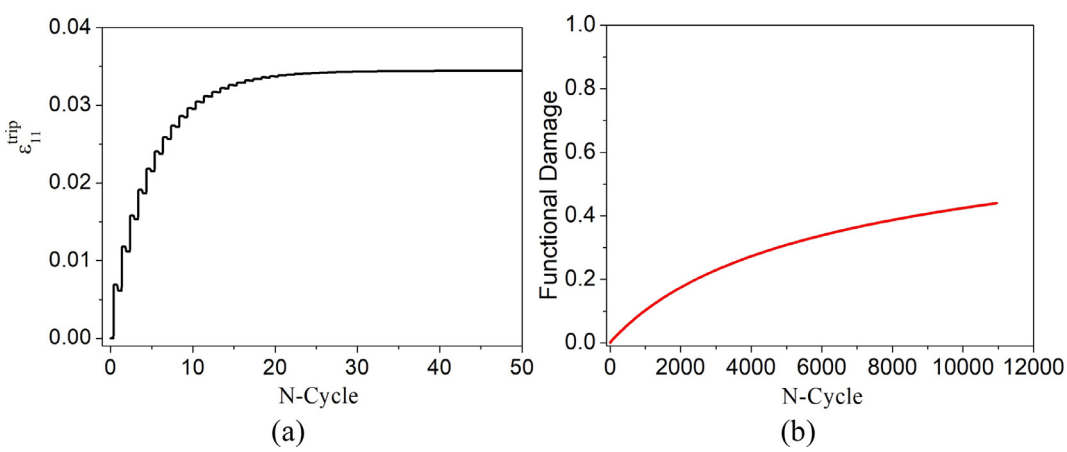

Fig. 7. TRIP strain and functional damage evolution during cyclic test for the evaluation of functional fatigue. (a) TRIP strain evolution; (b) functional damage evolution.

phase transformation capacity as shown in Fig. 6(a). For the 1000th cycle shown in Fig. 6(b), the material presents around 80% of the value initially observed and decreases this percentage over the cycles. In the 5,000th cycle, Fig. 6(c), approximately 50% of phase transformation capacity and finally, the cycle 10,955th, Fig. 6(d), presents around 30%. This result shows the influence of functional damage and TRIP in the material adaptive behavior that loses its performance over the cycles.

The evolution of TRIP strain and damage is presented in Fig. 7. The first 50 cycles of TRIP strain are shown in Fig. 7(a). It is observed that the material undergoes a rapid stabilization, where TRIP strain reaches a constant value, around 25 cycles, defining a stabilized stress-strain loop. On the other hand, Fig. 7(b) presents the evolution of the functional damage, showing that after 10,955 cycles, the functional damage reaches a value of approximately 45% causing the loss of functionality previously discussed. It should be pointed out that the damage variable tends to stabilize since phase transformation is dramatically reduced.

3.1. Thermal loadings

The functional fatigue due to thermal loadings is now in focus considering experimental results presented by Barrera et al. [33] and Azevedo et al. [17] as references. Barrera et al. [33] consider thermal cycles on a NiTi wire, initially in the austenitic phase, at a constant stress of 360 MPa. Upon cooling the sample, it undergoes austenite-

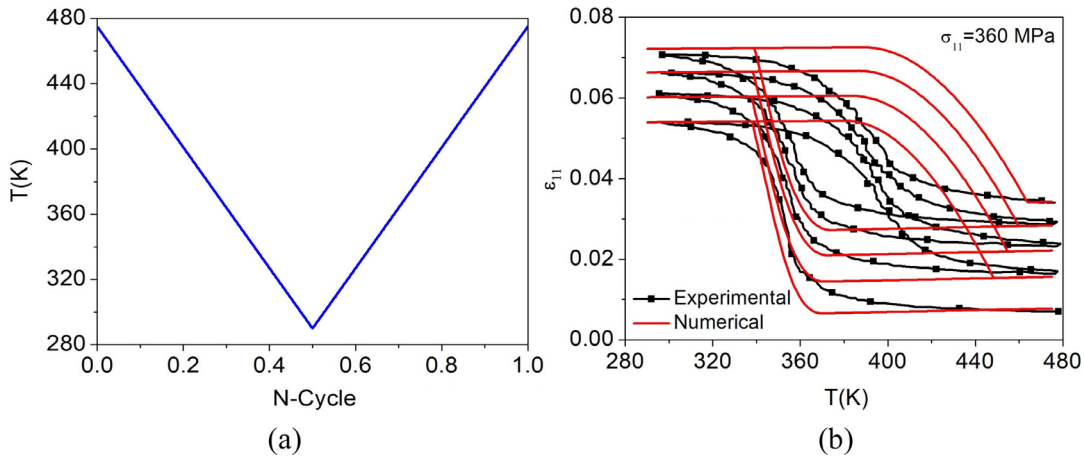

Fig. 8. Thermal cyclic test under a constant uniaxial load based on experimental tests due to Barrera et al. [33]: (a) thermal loading related to the first cycle; (b) strain-temperature curve obtained by numerical and experimental tests.

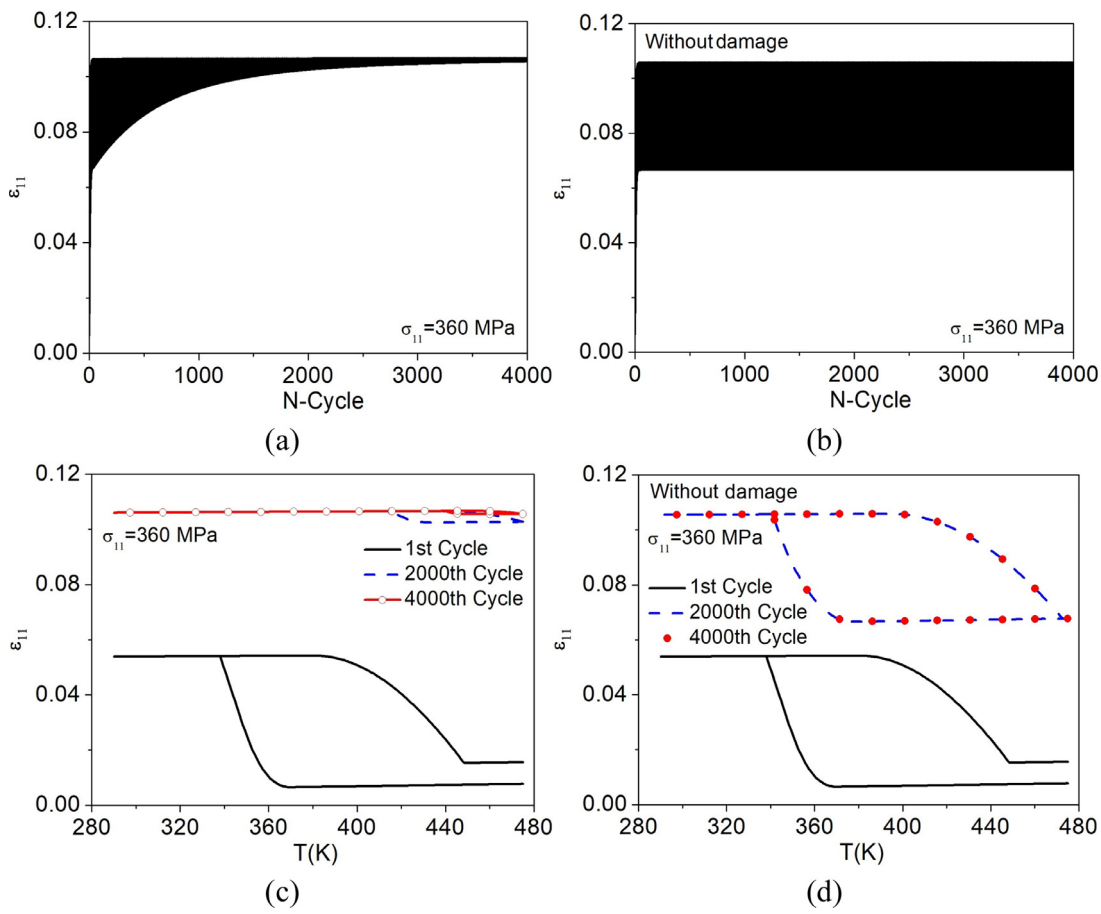

Fig. 9. Evolution of functional fatigue during thermal cyclic test considering a comparison between models with and without damage. (a) Evolution of the total strain with damage; (b) evolution of total strain without damage; (c) strain–temperature curve with damage; (d) strain–temperature curve without damage.

martensite transformation. By heating the wire, an inverse transformation is verified, returning to the austenitic phase. This process is presented in Fig. 8 showing numerical-experimental comparison considering adjusted parameters presented in Table 3 for numerical simulations. Once again, it is noticeable that the model captures the general behavior observed in experimental data, presenting a good agreement.

After this model verification, a set of numerical simulations is presented in the sequence. The first one corresponds to a cyclic test consisting of 4,000 thermal cycles, identical to that shown in Fig. 8(a), at a constant stress of 360 MPa. The influence of functional damage is evaluated considering a comparison between numerical simulations performed with and without functional damage, Fig. 9. Fig. 9(a) presents the evolution of the total strain considering the functional damage on the model, showing a progressive decrease of the strain amplitude through the cycles representing a loss of actuation performance. When the damage is neglected, it is observed the stabilization of the strain amplitude after some cycles, Fig. 9(b). A similar behavior can be observed in the strain-temperature curves, showed in Fig. 9(c)–(d). It should be pointed out

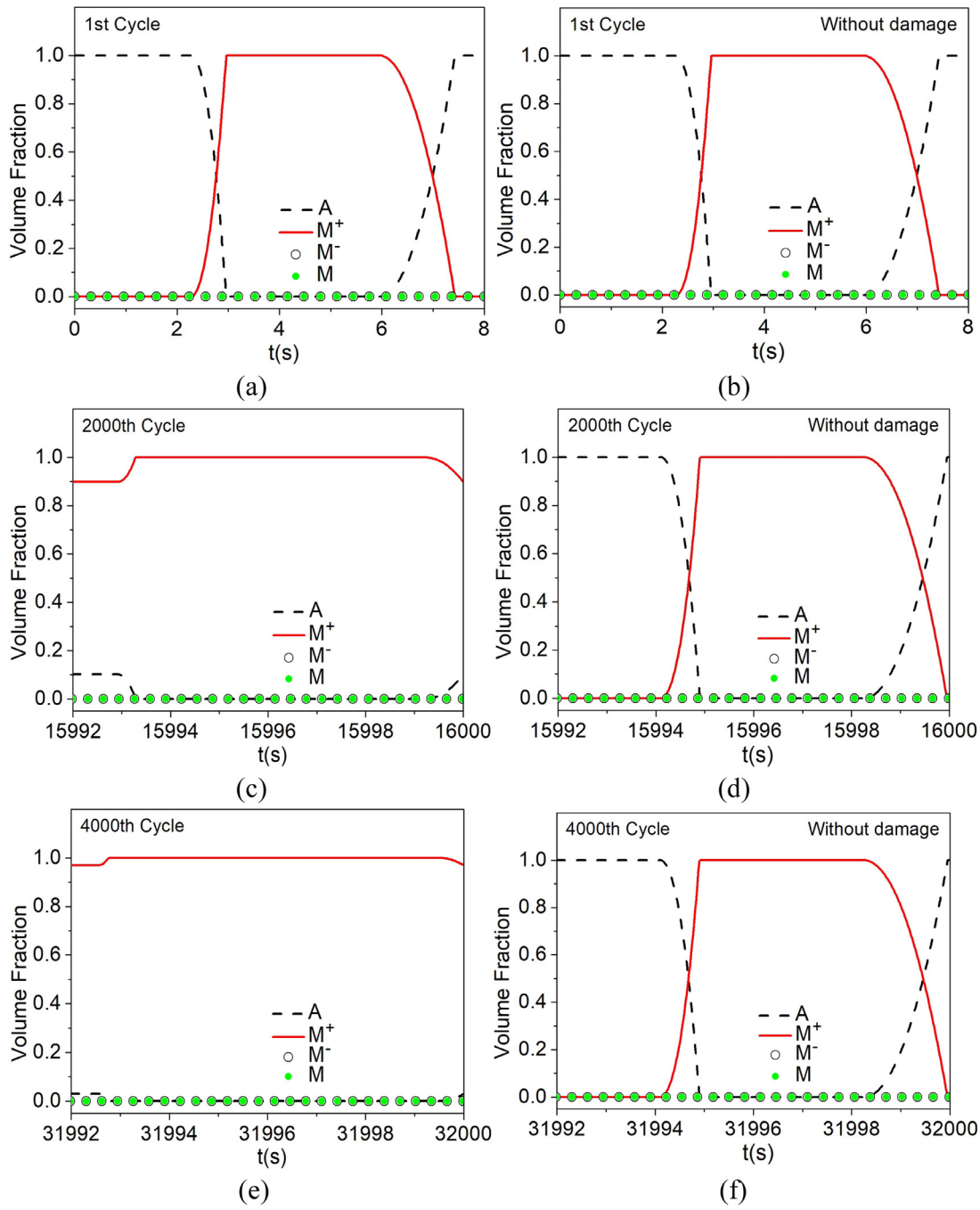

Fig. 10. Evolution of volume fractions during thermal cyclic test considering a comparison between models with and without damage. (a) 1st cycle with damage; (b) 1st cycle without damage; (c) 2,000th cycle with damage; (d) 2,000th cycle without damage; (e) 4,000th cycle with damage; (f) 4,000th cycle without damage.

that, when damage is neglected, TRIP evolution promotes the stabilization after a few cycles. When damage is considered, the SMA loses its capacity of phase transformation and as a result, a decrease of the hysteresis loop occurs.

Fig. 10 presents the time history of volume fractions showing details about phase transformations during this thermal loading process. Once again, the volume fractions of twinned martensite (M) and detwinned martensite induced by negative stress field (M^-) vanish due to the nature of the applied load. Note that in the 2,000th cycle, SMA has already lost around 90% of its phase transformation capacity, whereas for 4,000th cycle this value rises to approximately 95%. On the other hand, as expected, the lost of actuation is not observed when the damage is neglected.

The mechanical loading level is an important issue to define the SMA response during thermal cycles. Experimental tests presented by Azevedo et al. [17] consider the analysis of NiTi wires subjected to thermal loadings with different constant mechanical loads, showing that the loss of actuation performance is directly related to the mechanical loading level. Higher stress levels cause larger strains and tend to decrease SMA life as an actuator. In order to illustrate this behavior, consider a cyclic test consisting of 4,000 thermal cycles, similar to the one showed in Fig. 8(a), applying three different levels of constant mechanical load: 200 MPa, 300 MPa and 400 MPa. Fig. 11(a)–(b) shows the strain-temperature curves for 1st and 1,000th cycles, respectively. When the load of 200 MPa is applied, SMA presents a maximum strain around 4% without the occurrence of TRIP strain, and this value re-

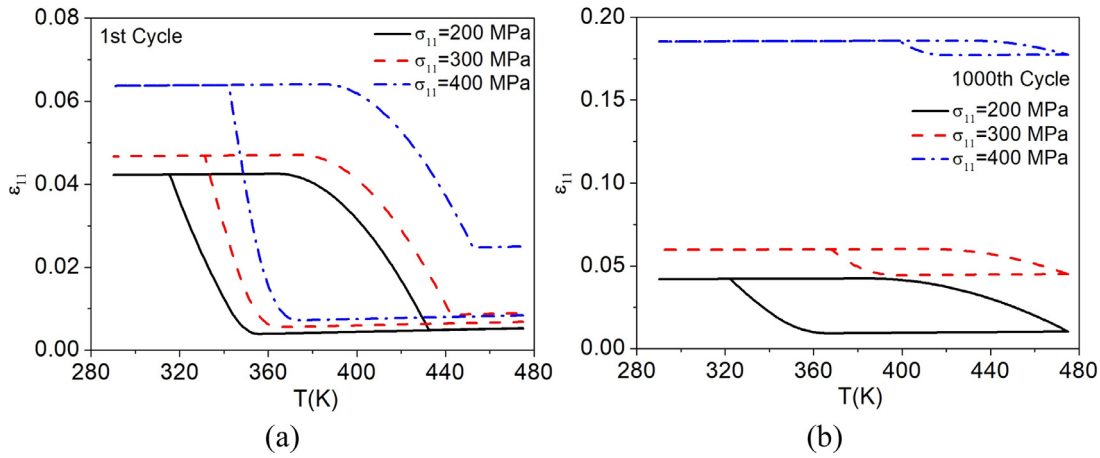

Fig. 11. Strain–temperature curves associated with cyclic functional fatigue tests for three different constant loads. (a) 1st cycle; (b) 1,000th cycle.

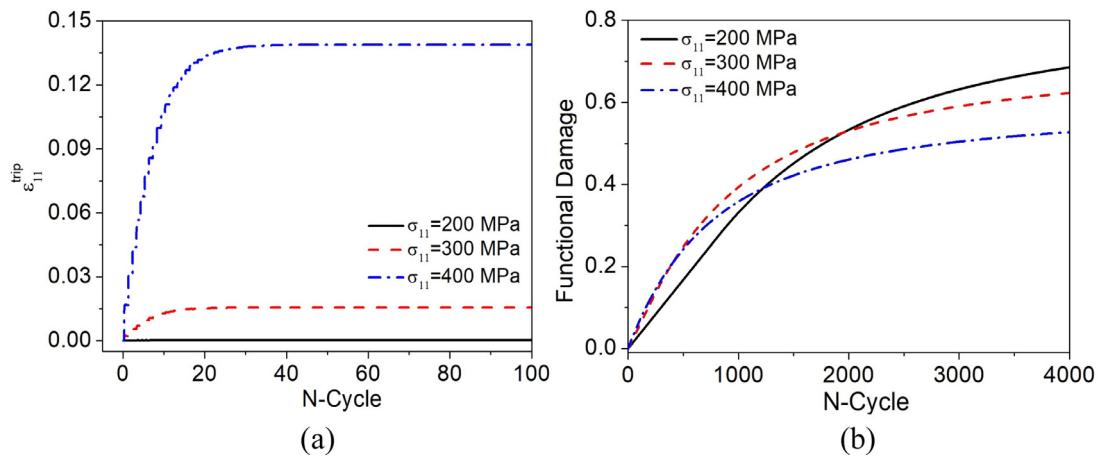

Fig. 12. Evolution of TRIP strain and functional damage during a cyclic functional fatigue test as a function of the applied load. (a) TRIP strain; (b) functional damage.

Table 3.
Parameters obtained from the experimental result proposed by Barrera et al. [33].

E^A(GPa)	E^M(GPa)	Ω^A(MPa/K)	Ω^M (MPa/K)	α_N^h(MPa)	$\hat{\alpha}$(MPa)
64.0	42.0	0.74	0.17	0.035	120.0
$\hat{L}_0^{\pm}$(MPa)	$\hat{L}^{\pm}$ (MPa)	$\hat{L}_0^A$(MPa)	$\hat{L}^A$ (MPa)	$(\eta_L)_N$(MPa.s)	$(\eta_U)_N$(MPa.s)
0.1	10.0	1.0	155.0	10.0	2.0
$(\eta_L^A)_N$ (MPa.s)	$(\eta_U^A)_N$(MPa.s)	T^M (K)	T^A (K)	σ_Y^M (GPa)	σ_Y^{Ai} (GPa)
10.0	2.0	342.0	413.0	1.0	2.0
σ_Y^{Af} (GPa)	K^A(GPa)	K^M(GPa)	H^A(GPa)	H^M (GPa)	η^l
1.5	1.4	0.4	4.0	1.1	− 0.01
η^K	T^F (K)	$\hat{M}_{13}$ (GPa^{-1})	$\hat{M}_{31}$(GPa^{-1})	$\hat{M}_{32}$(GPa^{-1})	$\hat{M}_{23}$ (GPa^{-1})
− 0.01	480.0	1.00	0.01	1.00	0.01
T^{trip}(K)	m^{α}	m^L	m^M	N	C_1
342.0	0.9	0.2	0.1	2	1×10^{-6}
C_2	C_3				
2×10^{-12}	1.2				

mains approximately constant for the first 1,000 cycles. When the load is 300 MPa, a similar behavior is verified, however, the presence of TRIP strain is verified in the first cycle and a greater decrease of the size of the hysteresis loop for 1,000th cycle is observed. Finally, when the load of 400 MPa is applied, an increase of the maximum strain is observed during the first cycle, as well as the value of the TRIP strain. For the last cycle, it is noticeable approximately 18% of maximum strain and a significant reduction in hysteresis loop size.

Fig. 12(a) shows the evolution of TRIP strain for the three load levels considering the first 100 cycles. Note that the TRIP is directly influenced by the applied stress and can vary approximately nine times when the load is increased from 300 to 400 MPa. On the other hand, the number of cycles for the stabilization does not vary significantly with the applied load, staying around thirty cycles for all the three cases. Figure 12 (b) shows the evolution of functional damage as a function of the mechanical load. In the first cycle, the wire has 100% of the phase transformation capacity for all conditions imposed. Larger loads generate a greater accumulation of functional damage over the thermal cycles causing a significant loss of actuation performance. Therefore, after a certain number of cycles, the material subjected to larger mechanical

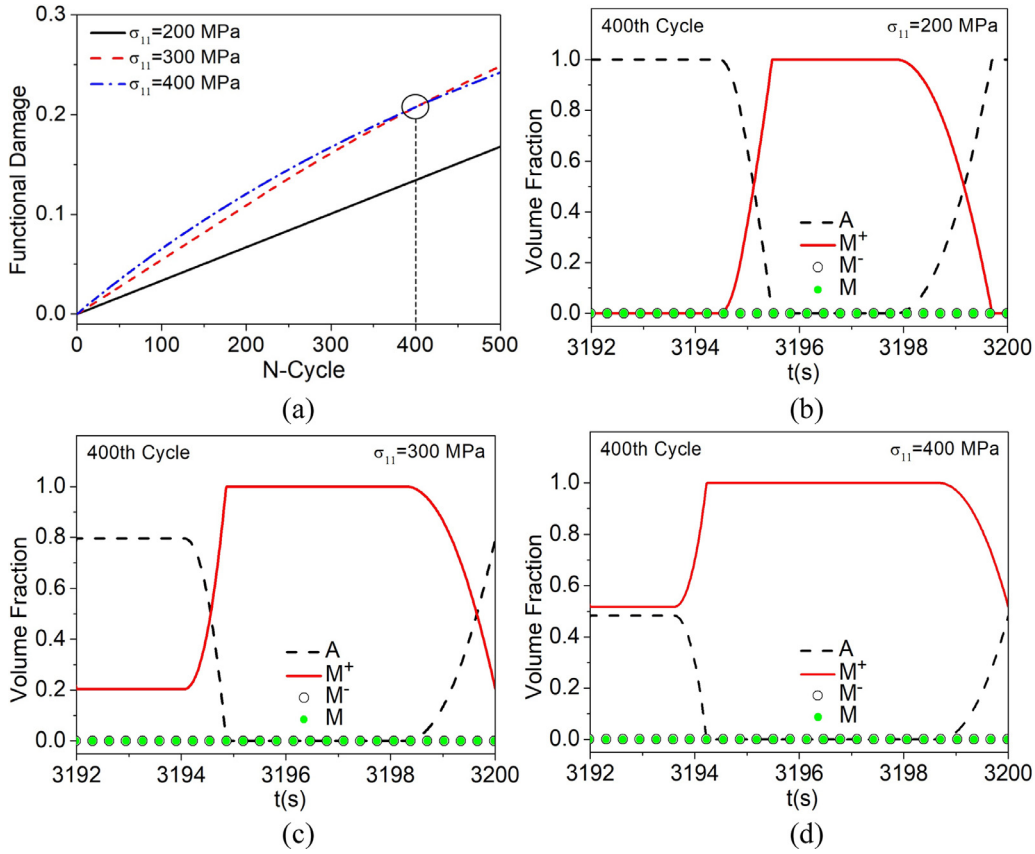

Fig. 13. Influence of the constant load during functional fatigue test considering the 400th cycle: (a) functional damage; (b) volume fraction for 200 MPa; (c) volume fraction for 300 MPa; (d) volume fraction for 400 MPa.

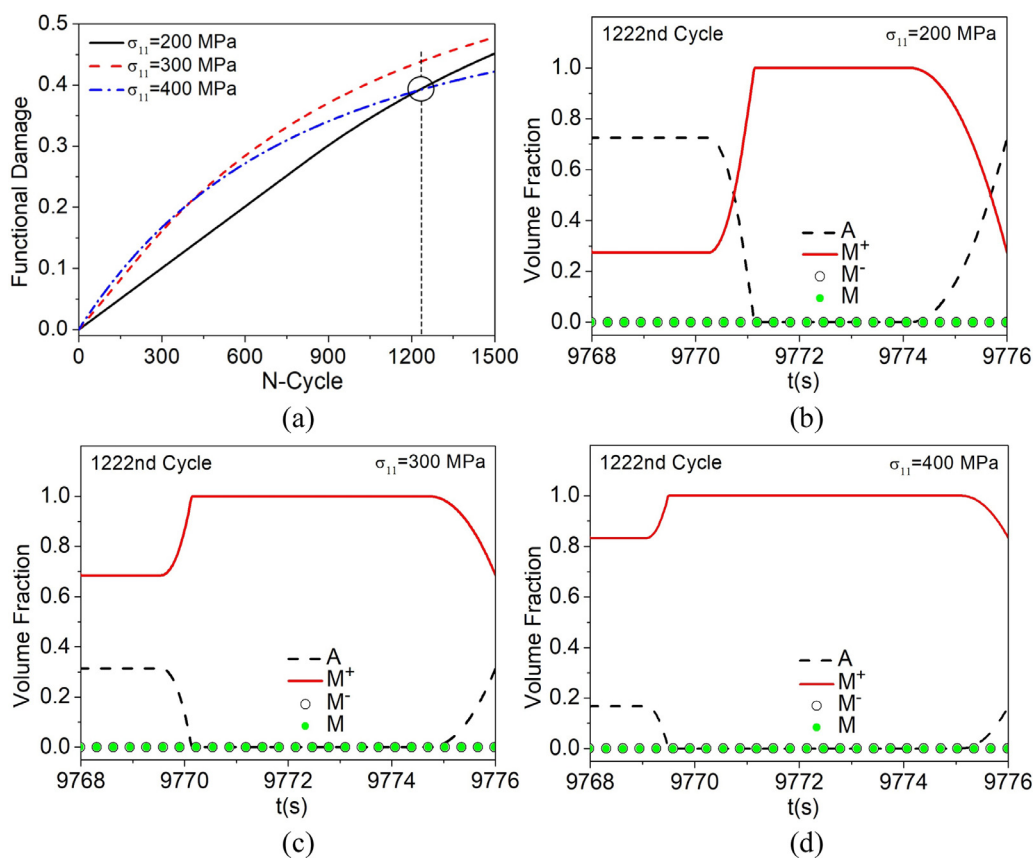

Fig. 14. Influence of the constant load during functional fatigue test considering the 1,222nd cycle: (a) functional damage; (b) volume fraction for 200 MPa; (c) volume fraction for 300 MPa; (d) volume fraction for 400 MPa.

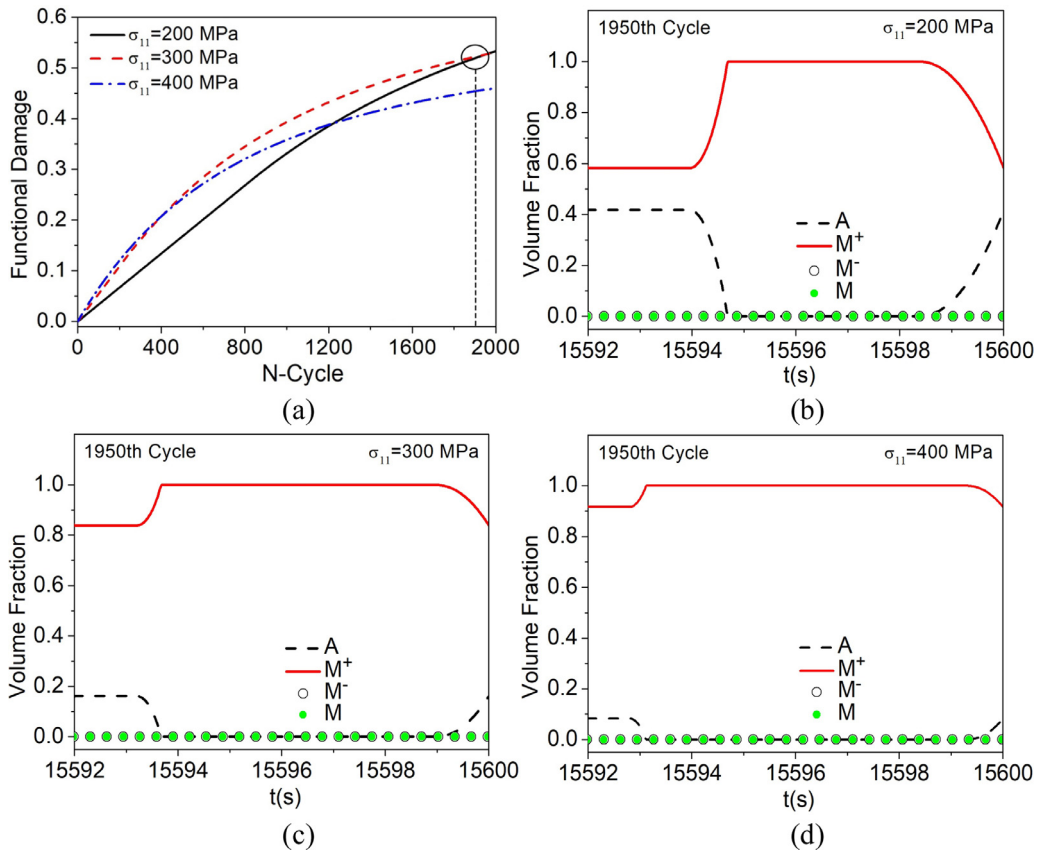

Fig. 15. Influence of the constant load during functional fatigue test considering the 1,950th cycle: (a) functional damage; (b) volume fraction for 200 MPa; (c) volume fraction for 300 MPa; (d) volume fraction for 400 MPa.

loads has already lost a larger portion of its performance and accumulates less damage than those under smaller loads.

In order to illustrate the relation between damage and phase transformation, a more specific analysis is now carried out. Fig. 13 presents the evolution of volume fractions for the 400th cycle. During the first 400 cycles, larger loads generate a greater accumulation of functional damage. For this cycle, the functional damage for 300 and 400 MPa is around 20%, while for 200 MPa it is approximately 13%. By observing the volume fraction evolution, it is noticeable that phase transformation is still the same when the load level is 200 MPa, but it loses approximately 20% and 50% of the phase transformation capacity, respectively for 300 and 400 MPa. By considering the 1,222nd cycle, Fig. 14, the damage evolution for 400 MPa assumes the same value as for 200 MPa, approximately 40%, while for the 300 MPa this value is around 45%. The evolution of the volume fractions for these loads shows a reduction of approximately 30%, 70% and 80%, respectively for the loads of 200, 300 and 400 MPa. Finally, by considering the 1,950th cycle, Fig. 15, the value of functional damage for 300 MPa equals that for 200 MPa, assuming the value of approximately 50%. On the other hand, the load of 400 MPa accumulates a functional damage of approximately 45%. The volume fractions for this cycle show that the material lost its phase transformation capacity about 60%, 80% and 90%, respectively, for 200, 300 and 400 MPa.

Based on these argues, it is possible to understand the reason for the loss of actuation performance, where the loading of 200 MPa promotes a greater accumulation of damage, reaching approximately 70% in 4,000th cycle, whereas for the other two higher level loads, it assumes approximately the values of 60% and 50% (for 300 and 400 MPa, respectively), as showed in Fig. 12(b).

Another way to evaluate the influence of applied mechanical loading on the material behavior is through the strain analysis during the cyclic loading. For this analysis, it is important to define the mean strain, $\bar{\varepsilon}_{11}$, and the strain amplitude, ε_A, based on the maximum strain, ε_{max}, and the residual strain, ε_{res}, as follows:

$$\bar{\varepsilon}_{11} = \frac{\varepsilon_{max} + \varepsilon_{res}}{2} \tag{51}$$

$$\varepsilon_A = \varepsilon_{max} - \varepsilon_{res} \tag{52}$$

Fig. 16 shows the functional damage analysis under the perspective of these new definitions. Once again, three levels of mechanical loads are of concern and the models with and without damage are presented. Two different pictures are presented for each variable, considering 4,000 cycles, and a zoom of the first 100 cycles. Fig. 16(a) presents the evolution of the maximum strain, showing that the load level increase, from 300 MPa to 400 MPa, causes the increase of the maximum strain by approximately three times. In addition, it is observed that the functional damage does not significantly alter the maximum value of the strain level. Fig. 16(b) shows the evolution of residual strain, highlighting the difference between the response with and without the functional damage as a function of loading level. When subjected to higher loads, there is a rapid evolution of functional damage during the first cycles, which produces the increase of the residual strain as shown in Fig. 16(b) for 400 MPa. On the other hand, the stress level of 300 MPa shows that the functional damage only changes the response, compared to the case without damage, approximately in the 250th cycle. When the stress level is 200 MPa, this change only occurs approximately in the 800th cycle. Fig. 16(c) shows the evolution of the mean strain and Fig. 16(d) shows the strain amplitude. It should be pointed out that a more pronounced decrease of the strain amplitude occurs for 400 MPa during the first cycles. This behavior is observed around the 1,000th when the stress level is 200 MPa.

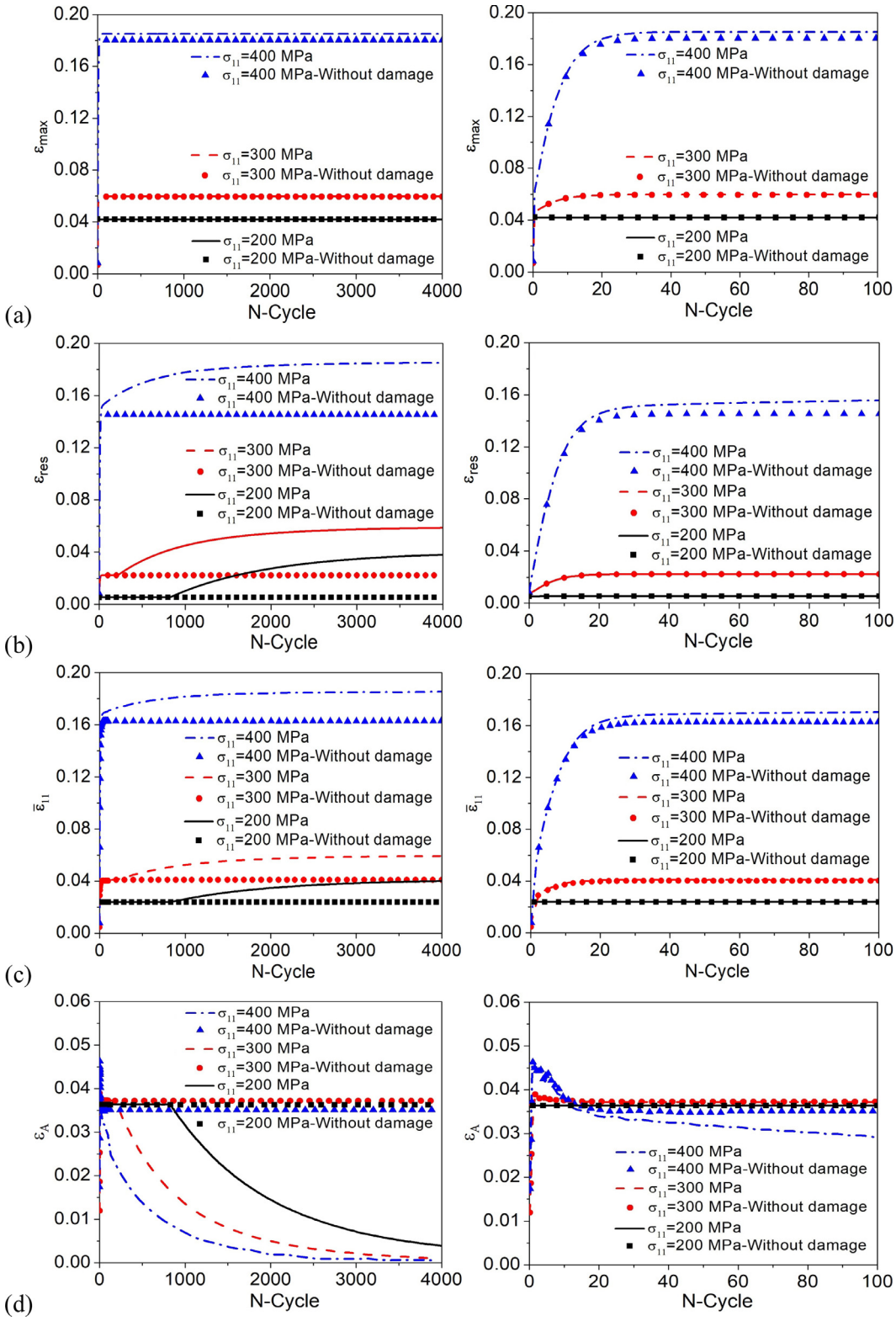

Fig. 16. Influence of the constant load during functional fatigue test comparing models with and without damage: (a) maximum strain; (b) residual strain; (c) mean strain; (d) strain amplitude.

4. Multiaxial tests

Numerical simulations developed for uniaxial test is a model verification based on experimental data, showing that it is capable to capture the general thermomechanical behavior of SMA functional fatigue. This section has the objective to extrapolate this analysis for multiaxial cases. A coupled tension-torsion test proposed by Sittner et al. [44] is considered as a reference, but they did not consider cyclic loading process. In brief, these tests consider NiTi wires subjected to a loading process presented in Fig. 17, being composed by a mechanical tensile loading (AB)

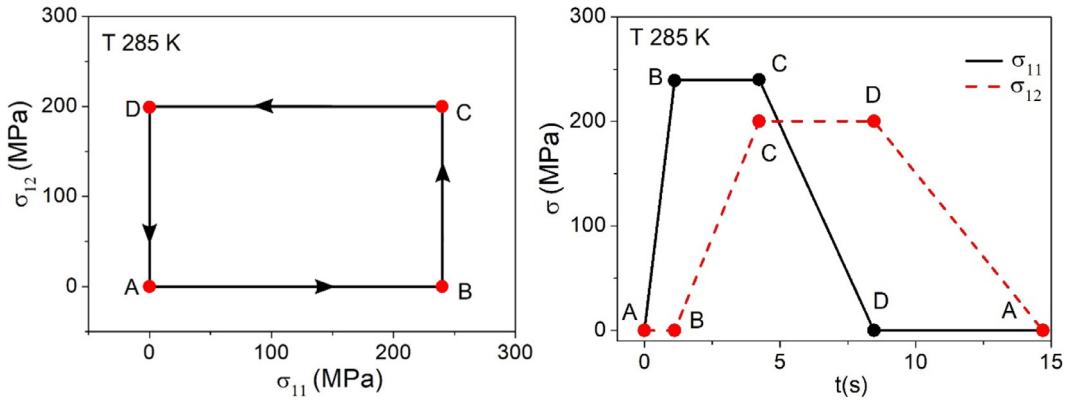

Fig. 17. Loading process of the coupled tension-torsion test.

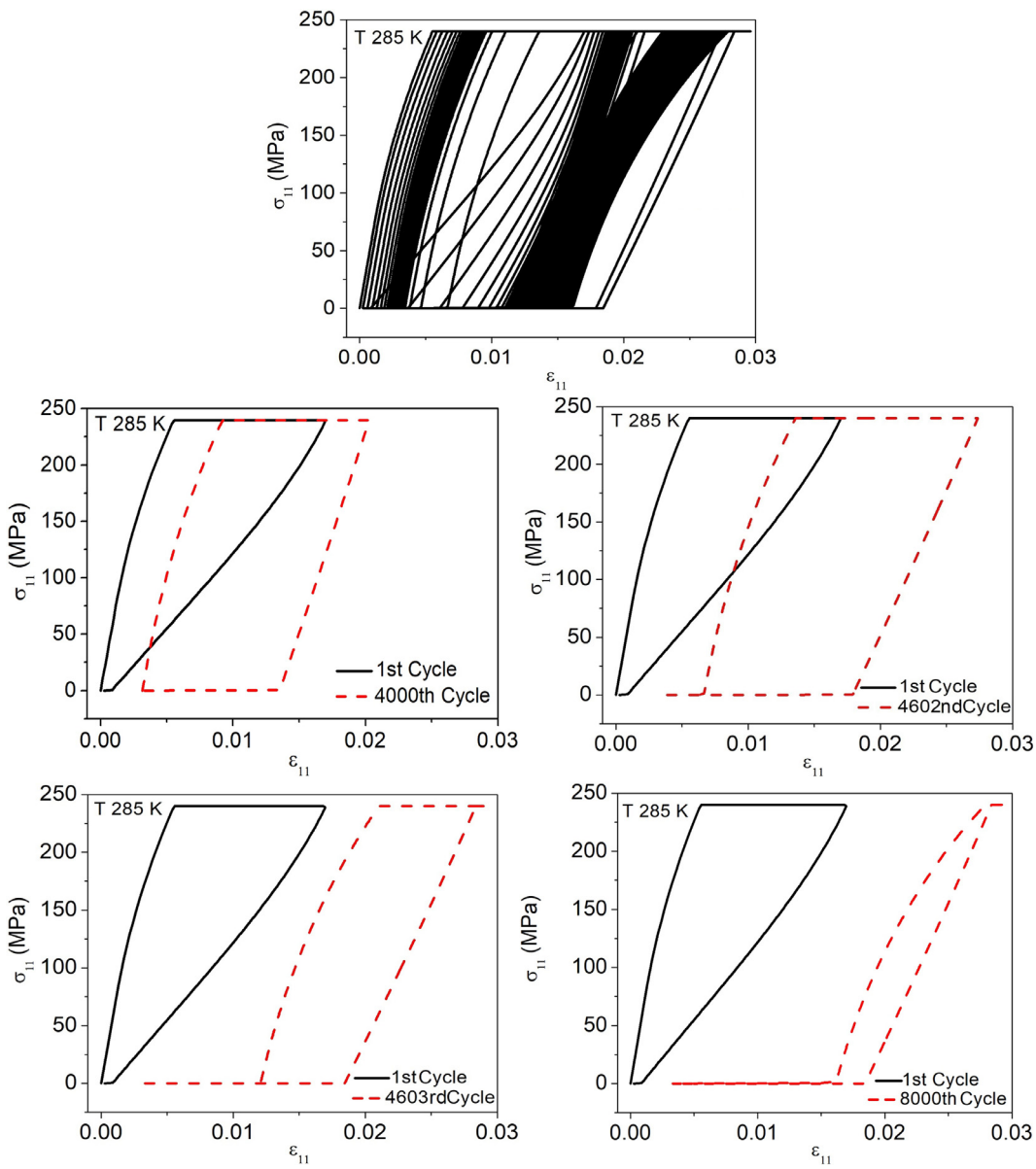

Fig. 18. Coupled tension-torsion cyclic loading test. Stress–strain curves, $\sigma_{11} \times \varepsilon_{11}$, for different cycles.

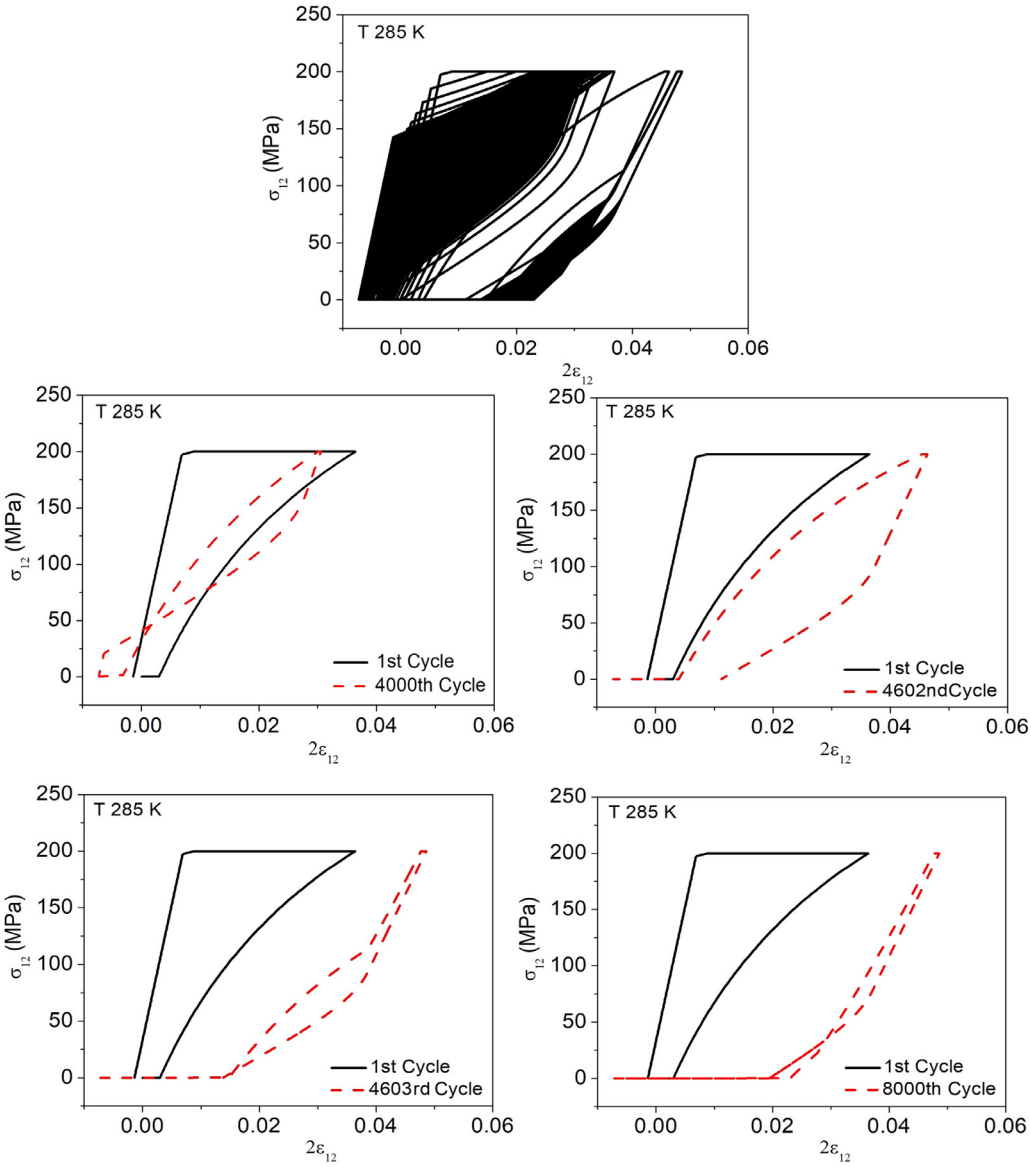

Fig. 19. Coupled tension-torsion cyclic loading test. Stress–strain curves, $\sigma_{12} \times 2\varepsilon_{12}$, for different cycles.

followed by a mechanical shear loading (BC) with load levels that are not enough to reach the yield surface. The unloading process starts with a tension unloading (CD) followed by a shear unloading (DA). Oliveira et al. [39] developed numerical simulations related to this experimental test without damage. The functional fatigue of multiaxial tests is now of concern, considering a cyclic loading process that repeats each one of these cycles. In general, 8000 cycles are considered, using parameters presented in Table 4.

Numerical simulations of 8,000 cycles are presented in Fig. 18 that shows the normal stress-strain curves ($\sigma_{11} \times \varepsilon_{11}$). Initially, all the 8,000 cycles are shown and then, four different cycles are presented illustrating the influence of the functional damage on the material response. The first cycle is always presented in order to allow one to perform a proper comparison. Note that there is a behavior transition between 4,602nd and 4,603rd cycles. Initially, the largest portion of phase transformation occurs when the axial and shear loads are applied together and the reverse phase transformation occurs mostly during the unloading of the normal stress. After the evolution of TRIP, the reverse transformation occurs mostly when the shear stress is unloaded. Functional damage evolution causes a behavior change where the reverse transformation occurs only when there is a small amount of shear strain. On the other hand, a reduction of the phase transformation capacity during the shear loading is observed for the direct transformation. This change promotes an increase on the maximum normal strain followed by a shape change of the stress-strain curve. After the 4,603rd cycle, a progressive reduction occurs in the area of the stress-strain curve, analogous to that observed for the uniaxial test, shown in Fig. 3. Fig. 19 presents shear stress-strain curves ($\sigma_{12} \times 2\varepsilon_{12}$) showing the same trends. Fig. 20 shows the normal-shear strain curves ($2\varepsilon_{12} \times \varepsilon_{11}$) and, once again, the same trends are observed.

A comparative analysis considering the model with and without damage is now in focus considering four distinct cycles. Fig. 21 presents normal stress-strain curves while Fig. 22 shows shear stress-strain curves. Normal-shear strain curves are presented in Fig. 23. It is noticeable that, after the 4,602nd cycle, the difference between both curves becomes more evident, showing a behavior change as a result of the evolution of functional damage.

Fig. 24 shows the evolution of the equivalent strain field, considering the number of cycles. Three regions are clearly identified: first cycles; transition zone; last cycles. During the first cycles, TRIP phenomenon

Table 4.
Parameters identified from the experimental results obtained by Sittner et al. [44].

E^A(GPa)	E^M(GPa)	Ω^A(MPa/K)	Ω^M (MPa/K)	α_N^h(MPa)	α_S^h(MPa)
65.0	29.0	0.74	0.17	0.0150	0.0160
$\hat{\alpha}$(MPa)	$\hat{L}_0^{\pm}$(MPa)	$\hat{L}^{\pm}$ (MPa)	$\hat{L}_0^A$(MPa)	$\hat{L}^A$ (MPa)	$(\eta_L)_N$(MPa.s)
140	1.50	5.00	2.00	26.00	5.70
$(\eta_U)_N$(MPa.s)	$(\eta_L^A)_N$(MPa.s)	$(\eta_U^A)_N$(MPa.s)	$(\eta_L)_S$(MPa.s)	$(\eta_U)_S$(MPa.s)	$(\eta_L^A)_S$(MPa.s)
12.00	25.00	3.50	4.85	14.00	10.00
$(\eta_U^A)_S$(MPa.s)	T^M (K)	T^A (K)	σ_Y^M (GPa)	σ_Y^{Ai} (GPa)	σ_Y^{Af} (GPa)
1.80	223.0	285.0	0.5	1.5	1.0
K^A(GPa)	K^M(GPa)	H^A(GPa)	H^M (GPa)	η^l	η^K
1.4	0.4	4.0	1.1	−0.01	−0.01
T^F (K)	$\hat{M}_{13}$ (GPa^{-1})	$\hat{M}_{31}$(GPa^{-1})	$\hat{M}_{23}$(GPa^{-1})	$\hat{M}_{32}$ (GPa^{-1})	T^{trip}(K)
423.0	0.072	0.071	0.072	0.071	270.0
m^α	m^L	m^M	N	υ^A	υ^M
0.07	0.20	0.14	2	0.36	0.36
C_1	C_2	C_3			
1×10^{-6}	2×10^{-12}	1.3			

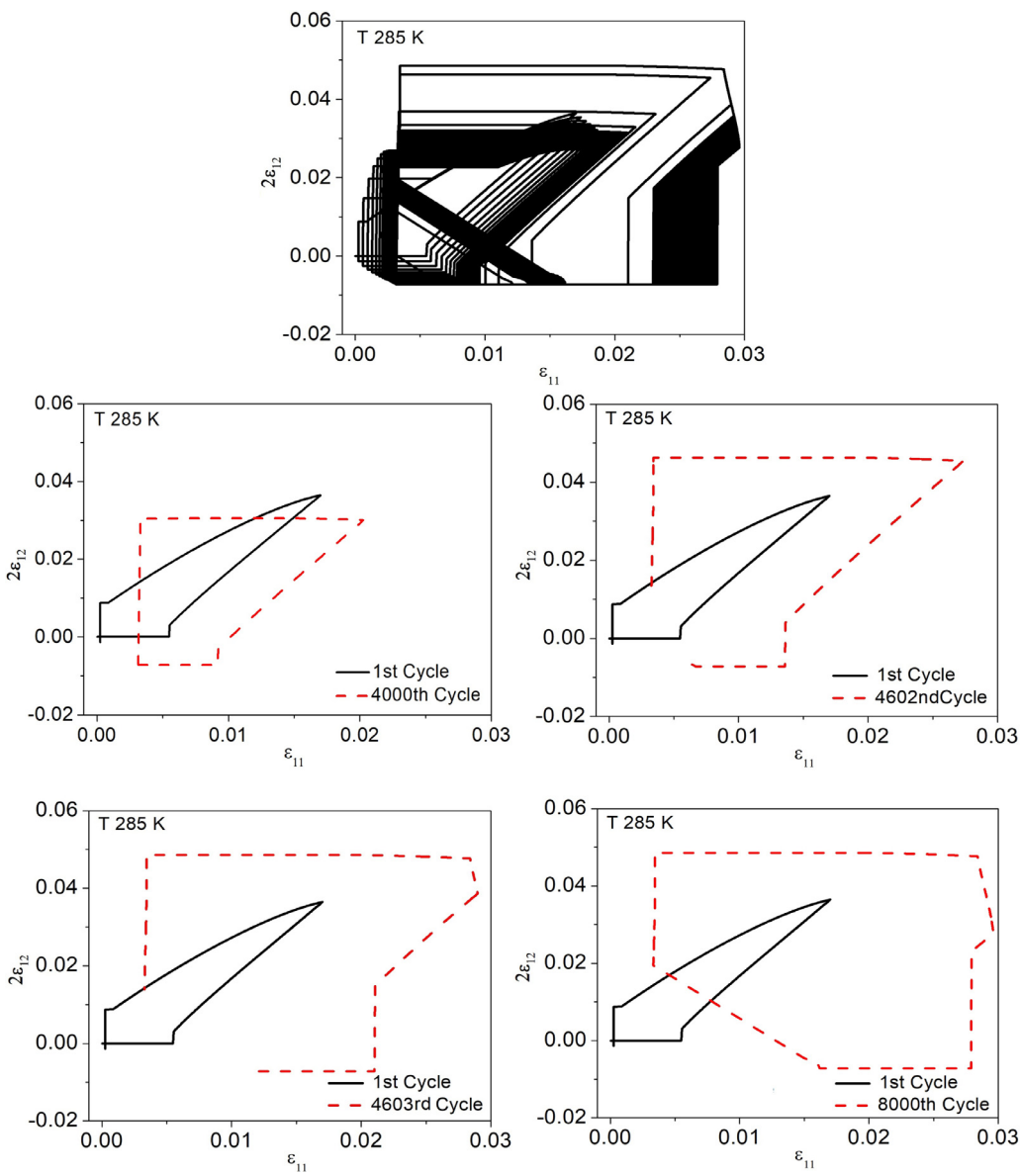

Fig. 20. Coupled tension–torsion cyclic loading test. Normal-shear strain curves, $2\varepsilon_{12} \times \varepsilon_{11}$, for different cycles.

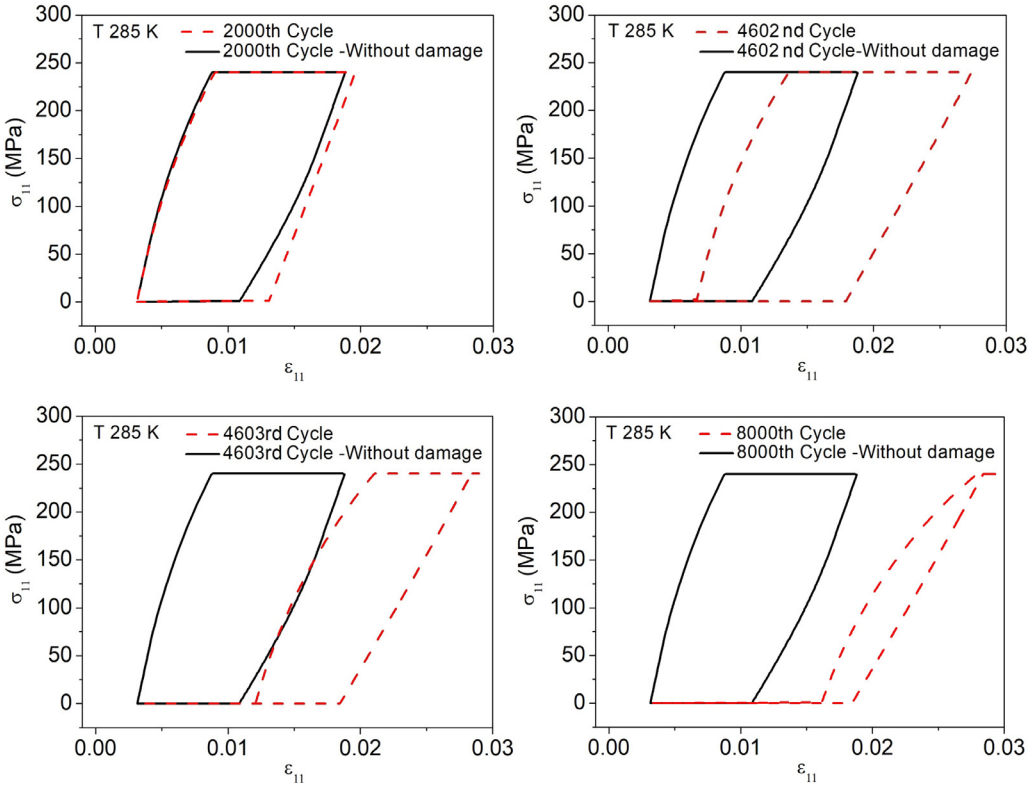

Fig. 21. Coupled tension-torsion cyclic loading test comparing models with and without damage. Stress–strain curves $\sigma_{11} \times \varepsilon_{11}$, for different cycles.

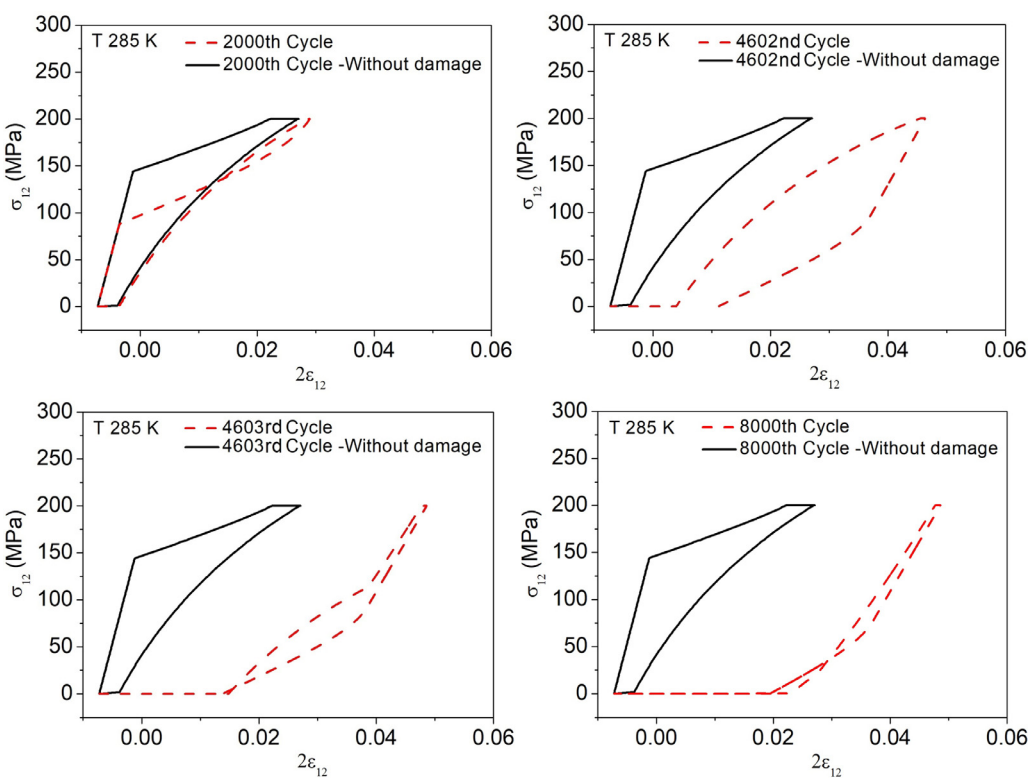

Fig. 22. Coupled tension-torsion cyclic loading test comparing models with and without damage. Stress–strain curves $\sigma_{12} \times 2\varepsilon_{12}$, for different cycles.

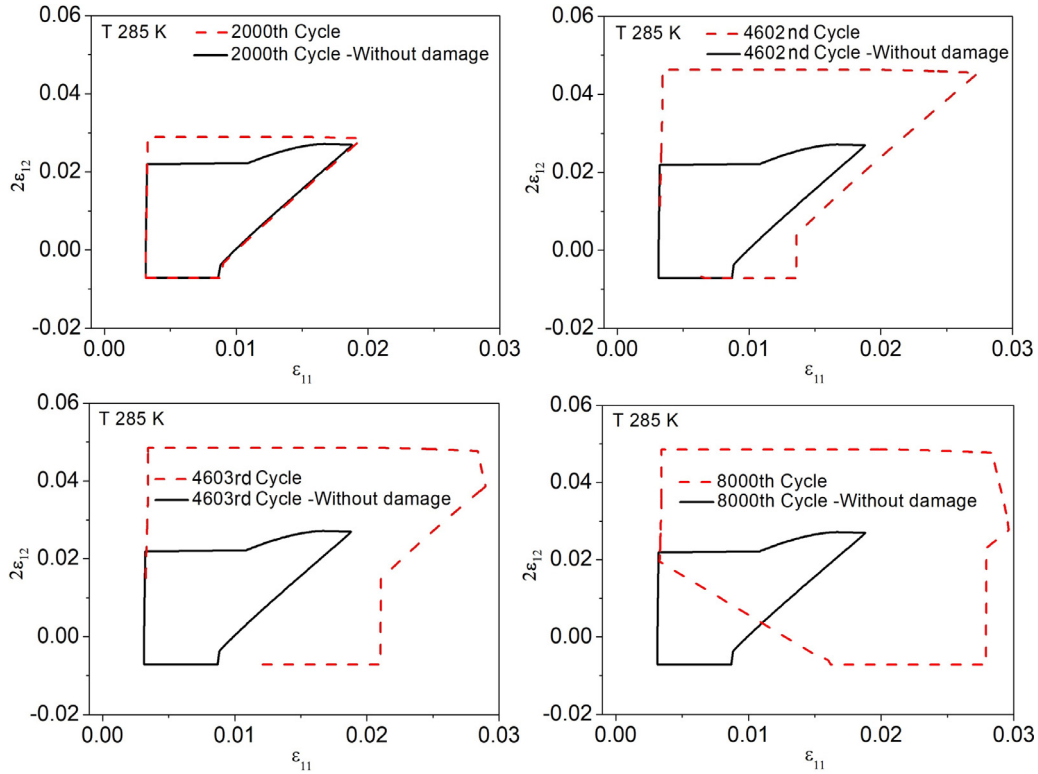

Fig. 23. Coupled tension-torsion cyclic loading test comparing models with and without damage. Strain curves $2\varepsilon_{12} \times \varepsilon_{11}$, for different cycles.

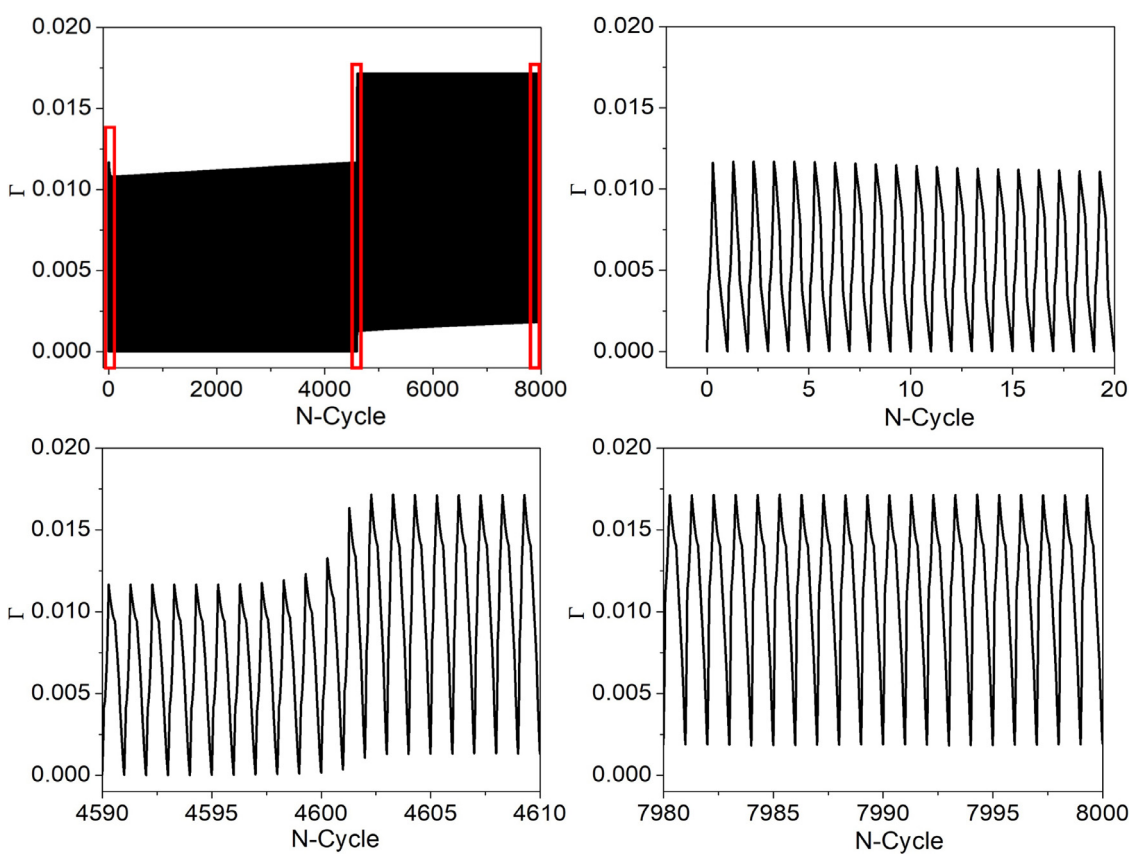

Fig. 24. Evolution of equivalent strain during functional fatigue test as a function of the number of cycles.

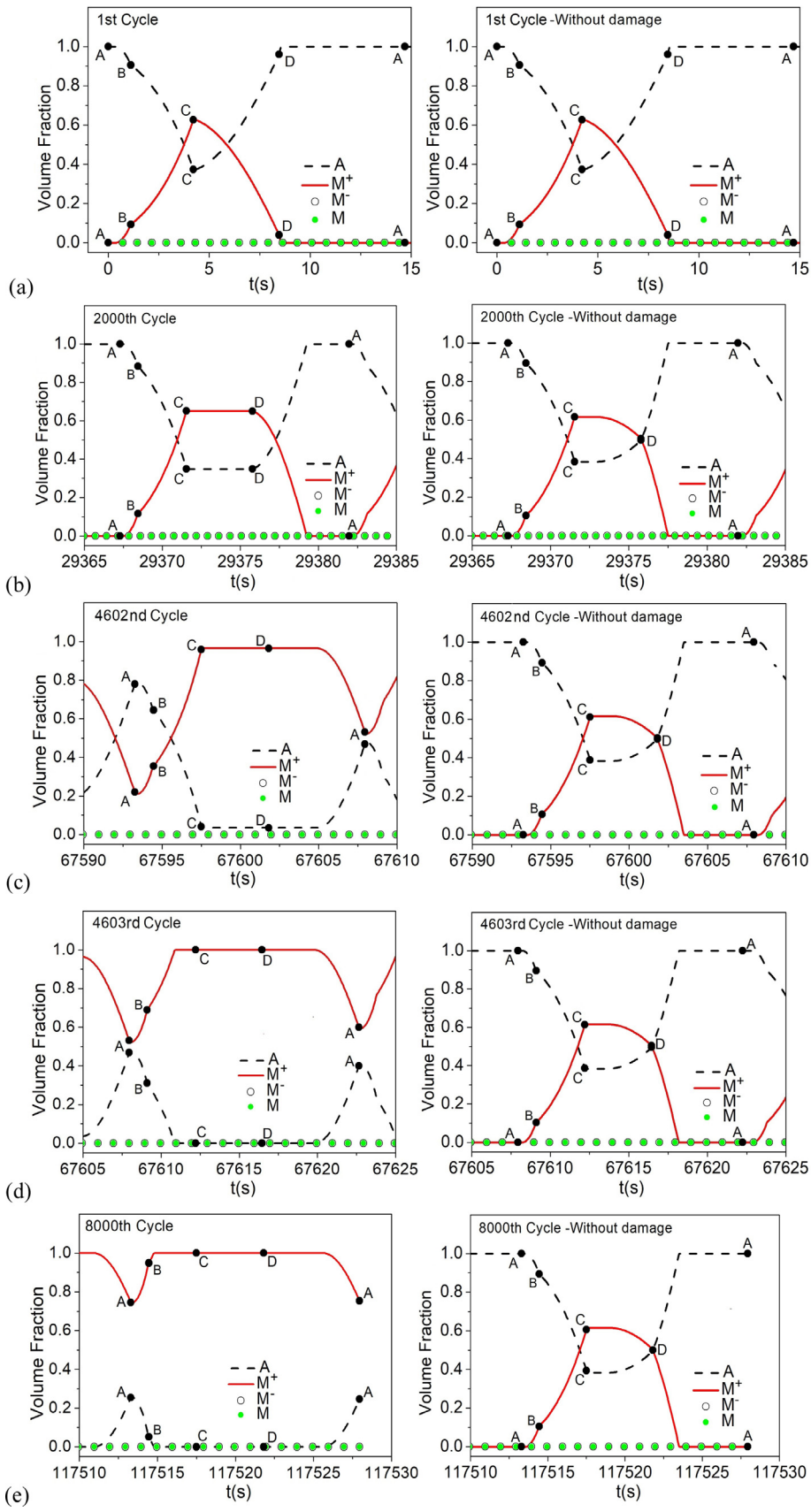

Fig. 25. Volume fraction evolution during the functional fatigue test for the model with and without damage. (a) 1st cycle; (b) 2,000th cycle; (c) 4,602nd cycle; (d) 4,603rd cycle; (e) 8,000th cycle.

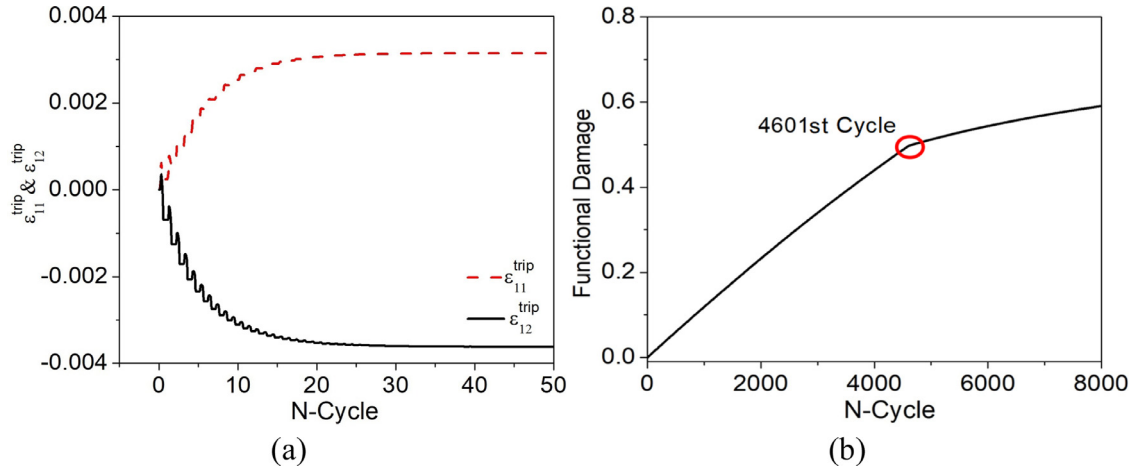

Fig. 26. Evolution of TRIP strain and functional damage during functional fatigue test. (a) TRIP strain; (b) functional damage.

is preponderant. During the transition zone, an abrupt increase of the maximum equivalent strain is observed. After this, values remain approximately constant.

The same comparison is now established by considering the evolution of volume fractions that allows one to verify phase transformation capacity, Fig. 25. For the first cycle shown in Fig. 25(a) it is observed that the phase transformation occurs as a function of the normal and shear loading and most of the volume fraction is formed when both normal and shear stresses are applied together. The reverse transformation starts at C and occurs mostly on CD. In the 2,000th cycle, Fig. 25(b), the TRIP strain is stabilized and no changes are observed in the case where the functional damage is neglected. When functional fatigue is incorporated into the analysis, damage evolution has the effect to delay the beginning of the reverse transformation. The consequence of delaying the reverse transformation process is an increase of the phase transformation capacity followed by a dramatic decrease after some cycles. Results show about 60% in the first cycle and about 80% in the 4,602nd cycle, shown in Fig. 25(a)– (c). After this, there is an abrupt reduction of the volume fractions as can be seen in 4,603rd cycle, where approximately 50% of the phase transformation capacity is achieved. After the transition zone, a progressive reduction of the phase transformation capacity is observed, assuming a value of approximately 30% in 8,000th cycle. The transition occurs when the functional damage reaches a stage that delays the reverse transformation DA (from 4,601st cycle to 4,603rd) in such a way that the direct transformation in the following cycles begins to increase during AB and reduce during BC, as can be seen by comparing the 4,602nd cycle, Fig. 25(c) and 4,603rd cycle, Fig. 25(d). The last cycles, after 4,603rd, show a progressive reduction of the amount of phase transformation observed during BC, Fig. 25(e), which shows the evolution of the volume fractions for the last cycle.

The evolution of TRIP and damage is now in focus, Fig. 26. TRIP evolution for the first 50 cycles is presented in Fig. 26(a). Note that saturation effect, which occurs around the 25th cycle, is related to a TRIP strain constant value. Fig. 26(b) shows the evolution of functional damage for the 8,000 cycles, highlighting the change of the evolution rate around the 4,601st cycle, representative of the transition zone.

5. Conclusions

This work presents a three-dimensional constitutive model to describe functional fatigue in shape memory alloys. The model is developed within the framework of generalized standard materials formalism, essentially based on thermodynamics, introducing a new state variable to describe the continuum functional damage based on phenomenological issues. A novel function is proposed to describe the continuum damage evolution being proportional to accumulated phase transformation and equivalent stress field. Numerical simulations are carried out comparing results with experimental data. Mechanical and thermal loadings are investigated and, in general, the model is capable to capture the main aspects of functional fatigue, being in close agreement with uniaxial experimental tests. After the uniaxial model verification, numerical simulations are performed considering multiaxial tests. Different loading conditions are investigated. Results show interesting responses, presenting three typical regions: first cycles; transition zone; last cycles. During the first cycles the evolution and stabilization of TRIP phenomenon are observed. After this stage, due to the evolution of the functional damage, a transition zone characterized by shape change in the stress-strain curves and by an abrupt increase on the maximum equivalent strain field occur. In addition, a progressive reduction in the hysteresis loop of the stress-strain curves is observed, similar to that observed for the uniaxial tests. It should be pointed out that phase transformations are dramatically reduced in the last cycles, representing the final stage of the lost of actuation. The developed simulations allow one to have a proper comprehension of functional fatigue, showing the phenomenological mechanisms behind the main effects.

Declaration of Competing interests

The author(s) declared no potential conflicts of interest with respect to the research, authorship, and/or publication of this article.

CRediT authorship contribution statement

Vanderson M. Dornelas: Conceptualization, Methodology, Software, Validation, Formal analysis, Investigation, Writing - original draft. **Sergio A. Oliveira:** Conceptualization, Methodology, Software, Validation, Formal analysis, Investigation, Writing - original draft. **Marcelo A. Savi:** Conceptualization, Methodology, Software, Validation, Formal analysis, Investigation, Writing - original draft, Supervision, Writing - review & editing.

Acknowledgments

The authors would like to acknowledge the support of the Brazilian Research Agencies CNPq, FAPERJ and CAPES (Grant PROEX 803/2018). The Air Force Office of Scientific Research (AFOSR) is also acknowledged.

References

[1] Lagoudas DC. Shape memory alloys: modeling and engineering applications. Department of Aerospace Engineering Texas A&M University, Springer Science Business Media, LLC; 2008.

[2] Leo DJ. Engineering analysis of smart material systems. New Jersey: John Wiley and Sons; 2007.
[3] Jani JM, Leary M, Subic A, et al. A review of shape memory alloy research, applications and opportunities. Mater Des 2014;56:1078–113.
[4] Cisse C, Zaki W, Zineb TB. A review of modeling techniques for advanced effects in shape memory alloy behavior. Smart Mater Struct 2016;25:1–36 a.
[5] Patoor E, Lagoudas DC, Entchev PB, et al. Shape memory alloys, part I: general properties and modeling of single crystals. Mech Mater 2006;38:391–429.
[6] Paiva A, Savi MA. An overview of constitutive models for shape memory alloys. Math Probl Eng 2006;2006:1–30.
[7] Khandelwal A, Buravalla V. Models for shape memory alloy behavior: an overview of modeling approaches. Int J Struct Changes Solids 2009;1(1):111–48.
[8] Cisse C, Zaki W, Zineb TB. A review of constitutive models and modeling techniques for shape memory alloys. Int J Plast 2016;76:244–84 b.
[9] Elahinia MH. Shape memory alloy actuators: design, fabrication, and experimental evaluation. New York: John Wiley & Sons Ltd; 2016.
[10] Eggeler G, Hornbogen E, Yawny A, et al. Structural and functional fatigue of NiTi shape memory alloys. Mater Sci Eng 2004;378:24–33.
[11] Tobushi H, Hachisuka T, Hashimoto T, et al. Cyclic deformation and fatigue of a TiNi shape-memory alloy wire subjected to rotating bending. ASME J Eng Mater Technol 1998;120:64–70.
[12] Figueiredo AM, Modenesi P, Buono V. Low-cycle fatigue life of superelastic NiTi wires. Int J Fatigue 2009;31(4):751–8.
[13] Kang G, Kan Q, Yu C, et al. Whole-life transformation ratchetting and fatigue of super-elastic NiTi alloy under uniaxial stress-controlled cyclic loading. Mater Sci Eng A 2012;535:228–34.
[14] Song D, Kang G, Kan Q, et al. Non-proportional multiaxial whole-life transformation ratchetting and fatigue failure of super-elasticNiTishape memory alloy micro-tubes. Int J Fatigue 2015;80:372–80.
[15] Lagoudas DC, Miller DA, Rong L, et al. Thermomechanical fatigue of shape memory alloys. Smart Mater Struct 2009;18(8):1–12.
[16] Bertacchini OW, Lagoudas DC, Patoor E. Thermomechanical transformation fatigue of TiNiCu SMA actuators under a corrosive environment – Part I: experimental results. Int J Fatigue 2009;31(10):1571–8.
[17] Azevedo AJM, Paixão RB, Rentes RB, et al. Device for fatigue analysis of shape memory alloy wires. In: Proceedings of the twenty-third ABCM international congress of mechanical engineering – COBEM 2015. Rio de Janeiro: ABCM; 2015.
[18] Ramos ADO, de Araújo CJ, de Oliveira HMR, et al. An experimental investigation of the superelastic fatigue of NiTi SMA wires. J Braz Soc Mech Sci Eng 2018;40:1–14.
[19] Zheng L, Yongjun H, Moumni Z. Investigation on fatigue behaviors of NiTi polycrystalline strips under stress-controlled tension via in-situ macro-band observation. Int J Plast 2017;90:116–45.
[20] Pelton AR. Nitinol fatigue: a review of microstructures and mechanisms. J Mater Eng Perform 2011;20(4):613–17.
[21] Tobushi H, Nakahara T, Shimeno Y, et al. Low-cycle fatigue of TiNi shape memory alloy and formulation of fatigue life. ASME J Eng Mater Technol 1999;122(2):186–91.
[22] Runciman A, Xu D, Pelton AR, et al. An equivalent strain/Coffin–Manson approach to multiaxial fatigue and life prediction in superelastic nitinol medical devices. Biomaterials 2011;32(22):4987–93.
[23] Maletta C, Sgambitterra E, Furgiuele F, et al. Fatigue of pseudoelastic NiTi within the stress-induced transformation regime: a modified Coffin–Manson approach. Smart Mater Struct 2012;21(11):112001.
[24] Kollerov M, Lukina E, Gusev D, et al. Impact of material structure on the fatigue behaviour of NiTi leading to a modified Coffin–Manson equation. Mater Sci Eng: A 2013;585:356–62.
[25] Moumni Z, Herpen AV, Riberty P. Fatigue analysis of shape memory alloys: energy approach. Smart Mater Struct 2005;14(5):S287–92.
[26] Kan Q, Kang G, Yan W, et al. An energy-based fatigue failure model for super-elastic NiTi alloys under pure mechanical cyclic loading. In: Proceedings of the SPIE 8409, third international conference on smart materials and nanotechnology in engineering, 8409, 84090F; 2012.
[27] Zhang Y, Zhu J, Moumni Z, et al. Energy-based fatigue model for shape memory alloys including thermomechanical coupling. Smart Mater Struct 2016;25(3):035042.
[28] Zhang Y, You Y, Moumni Z, et al. Experimental and theoretical investigation of the frequency effect on low cycle fatigue of shape memory alloys. Int J Plast 2017;90:1–30.
[29] Zhang Y, You Y, Moumni Z, et al. Stored-energy-based fatigue criterion for shape memory alloys. Smart Mater Struct 2019;28(6):065027.
[30] Song D, Kang G, Kan Q, et al. Damage-based life prediction model for uniaxial low-cycle stress fatigue of super-elastic NiTi shape memory alloy microtubes. Smart Mater Structures 2015;24(8):085007.
[31] Song D, Kang G, Yu C, et al. Non-proportional multiaxial fatigue of super-elastic NiTi shape memory alloy micro-tubes: damage evolution law and life-prediction model. Int J Mech Sci 2017;131–132:325–33.
[32] Hartl DJ, Chemisky Y, Meraghni F. Three-dimensional constitutive model considering transformation-induced damage and resulting fatigue failure in shape memory alloys. Proc SPIE 2014;9058:905805.
[33] Barrera N, Biscari P, Urbano MF. Macroscopic modeling of functional fatigue in shape memory alloys. Eur J Mech A/Solids 2014;45:101–9.
[34] Zhang X, Huang D, Yan X, et al. Modeling functional fatigue of SMA using a more accurate subdivision of martensite volume fractions. Mech Mater 2016;96:12–29.
[35] Bartel T, Osman M, Menzel A. A phenomenological model for the simulation of functional fatigue in shape memory alloy wires. Meccanica 2017;52(4):973–88.
[36] Chemisky Y, Darren JH, Fodil M. Three-dimensional constitutive model for structural and functional fatigue of shape memory alloy actuators. Int J Fatigue 2018;112:263–78.
[37] Phillips FR, Wheeler RW, Geltmacher AB, et al. Evolution of internal damage during actuation fatigue in shape memory alloys. Int J Fatigue 2019;124:315–27.
[38] Oliveira SA, Savi MA, Zouain N. A three-dimensional description of shape memory alloy thermomechanical behavior including plasticity. J Braz Soc Mech Sci Eng 2016;38(5):1451–72.
[39] Oliveira SA, Dornelas VM, Savi MA, et al. A phenomenological description of shape memory alloy transformation induced plasticity. Meccanica 2018;53(10):2503–23.
[40] Lemaitre J, Chaboche JL. Mechanics of solid materials. New York: Cambridge University Press; 1990.
[41] Coleman BD, Gurtin ME. Thermodynamics with internal state variables. J Chem Phys 1967;47(2):597–613.
[42] Paiva A, Savi MA, Braga MB, et al. A constitutive model for shape memory alloys considering tensile-compressive asymmetry and plasticity. Int J Solids Struct 2005;42:3439–57.
[43] Ortiz M, Pinsky PM, Taylor RL. Operator split methods for the numerical solution of the elastoplastic dynamic problem. Comput Methods Appl Mech Eng 1983;39(2):137–57.
[44] Sittner P, Hara Y, Tokuda M. Experimental study on the thermoelastic martensitic transformation in shape memory alloy polycrystal induced by combined external forces. Metall Mater Trans A 1995;26(11):2923–35.